

Check for updates

# **Engineering Drug-Eluting Ocular Bioadhesive "OcuTAPE"** via Tannic Acid-Mediated Nanoparticle Bridging

Yuting Zheng, Monu Monu, Steven Vo, Suneel Gupta, Lal Krishan Kumar, Prince Kumar, Nariman Nassiri, Pawan Kumar Singh,\* and Nasim Annabi\*

Dynamic integration of nanoparticles (NPs) into hydrogels remains a key challenge in engineering drug-eluting bioadhesives. A generalizable strategy leveraging the multifunctional binding capacity of tannic acid (TA) to bridge drug-loaded NPs and hydrogel via hydrogen bonding is presented. Acting as both a bioadhesive moiety and dynamic crosslinker, TA enables synthesis-free NP incorporation and facilitates versatile nanocomposite designs for sustained, localized drug delivery. To demonstrate clinical relevance, a ready-to-use ocular patch named 'OcuTAPE' is developed to address the unmet need for bioadhesives that seal injuries and provide sustained drug release. Current ocular adhesives suffer from poor retention, mechanical mismatch, uncontrolled drug release, and limited usability. OcuTAPE achieves high toughness (≈4000 kJ m<sup>-3</sup>), rapid wet tissue adhesion without external aids, and TA-mediated integration of poly (ethylene glycol) (PEG)-based micelles (MCs) for dexamethasone (Dex) release over five weeks. The patch conforms to ocular biomechanics, retains in vivo on rabbit and pig eyes, and demonstrates biocompatibility and intrinsic anti-inflammatory efficacy. To illustrate TA-bridging versatility, a second model with drug-loaded poly (lactic-co-glycolic acid) (PLGA) NPs in a gelatin methacryloyl (GelMA)-TA hydrogel is engineered, serving as a naturally derived matrix suitable for tissue regeneration. These findings establish TA bridging as a robust strategy for engineering drug-eluting nanocomposite bioadhesives, with OcuTAPE as a clinically relevant model.

drug delivery. These systems integrate the advantages of both NPs, such as high drug loading capacity, tunable release kinetics, and protection of labile compounds, and hydrogels, which serve as biocompatible, tissue-conforming matrices for controlled release at target sites. However, a key limitation of current NP-hydrogel systems lies in the weak integration between the two components. Most formulations rely on physical encapsulation,[1] which often leads to premature NP release, early-stage drug loss, and potential toxicity, especially in sensitive environments like the eye.[2] Preleaching issues are further exacerbated by low crosslinking density and high swelling of hydrogels in wet conditions.[2] Although chemically modified nanomaterials or hydrogel prepolymers have been used to immobilize NPs for extended drug release,[3] these methods often involve complex synthesis steps and may introduce harmful substances, making them less suitable for delicate applications. Therefore, there is a critical need for a straightforward, synthesis-free, and biocompatible strategy that uses naturally derived components to stably incorporate drugloaded NPs into hydrogel networks. This approach enables prolonged drug retention and controlled

#### 1. Introduction

Drug-loaded nanoparticle (NP)-hydrogel hybrid systems have emerged as a promising platform for localized and sustained approach enables prolonged drug retention and controlled release without compromising biosafety or formulation simplicity.

Y. Zheng, S. Vo, N. Annabi
Department of Chemical and Biomolecular Engineering
University of California, Los Angeles
Los Angeles, California 90095, USA
E-mail: nannabi@ucla.edu

M. Monu, L. K. Kumar, P. Kumar, P. K. Singh Department of Ophthalmology Mason Eye Institute University of Missouri School of Medicine Columbia, MO 65201, USA

The ORCID identification number(s) for the author(s) of this article can be found under https://doi.org/10.1002/adfm.202516281

DOI: 10.1002/adfm.202516281

E-mail: pksfcq@health.missouri.edu

S. Gupta Harry S. Truman Memorial Veterans' Hospital

S. Gupta

Departments of Veterinary Medicine & Surgery and Biomedical Sciences College of Veterinary Medicine

University of Missouri Columbia, MO 65211, USA

Columbia, MO 65201, USA

Columbia, MO 65211, USA N. Nassiri

Glaucoma Division Department of Ophthalmology UCLA Doheny Eye Institute Pasadena, CA 91105, USA

N. Annabi Department of Bioengineering University of California, Los Angeles Los Angeles, California 90095, USA



1616282.6, Downloaded from https://advanced.onlinelbing.wiley.com/doi/10.1002/adfm.202516281 by University Of California, Los Angeles, Wiley Online Library on [22:08:2025]. See the Terms and Conditions (https://onlinelbitrary.viety.com/terms-and-conditions) on Wiley Online Library for rules of use; OA archies are governed by the applicable Centwise Commons I

www.afm-journal.de

Among localized drug delivery systems, ocular bioadhesives present a particularly demanding yet clinically impactful application. Hydrogel-based adhesives offer biocompatibility, high water content, and mechanical flexibility,[4] and have shown potential advantages over traditional sutures in certain applications. [5] Recent efforts have focused on improving their adhesive strength, durability, and clinical usability; however, challenges remain in optimizing wet tissue adhesion, sustained drug release, and mechanical properties. Existing bioadhesive hydrogels have utilized three in situ gelation mechanisms: temperature-responsive solgel transition,<sup>[6]</sup> photocrosslinking,<sup>[5,7]</sup> or component mixing.<sup>[8]</sup> However, these methods pose practical challenges. Temperatureresponsive hydrogels can gel unevenly in ambient air; photocrosslinking requires external light sources (e.g., UV light) that may damage ocular tissue; [7,9] and component-mixed systems often require precise control over pH, [6,10] temperature, [6,11] or addition of crosslinkers.<sup>[12]</sup> Furthermore, gelation kinetics are difficult to control as some systems polymerize too quickly,[12,13] complicating handling or causing clogging within the applicator, while others are too slow, [6,8,14] reducing efficiency. Liquid precursors may disperse on the curved tissue surfaces, and misplaced gels are difficult to reposition, limiting their utility in emergencies or resource-limited settings. Additionally, fresh preparation requirements hinder their long-term storage and scalability.

In addition to formulation challenges, mechanical properties are often insufficiently tuned. For example, many ocular adhesives are either too soft (<10 kPa)<sup>[6,7,12–15]</sup> or excessively stiff (with a Young's modulus greater than 200 kPa)[7,16] to match native conjunctival tissue. This mismatch causes discomfort, irritation, or an allergic response, [17] undermining compliance. Adequate toughness is also lacking, limiting resistance to blinking and ocular motion.[18] Natural blinking and eye movements can further disrupt cohesive and adhesive integrity, [19] and discomfort from mechanical mismatch may prompt premature removal by patients. Although progress has been made in enhancing the adhesive strength, long-term in vivo retention remains uncertain due to the distinct physiological challenges of the dynamic and lubricated ocular surfaces.<sup>[20]</sup> Few studies report consistent long-term retention without auxiliary support, such as Elizabethan collars to prevent animals from scratching off the material, [7] underscoring the need for adhesives with improved mechanical compatibility and retention.

Beyond mechanical and adhesive limitations, effective drugeluting ocular adhesives have yet to be realized. Due to the ocular environment, characterized by rapid tear turnover, blinking-induced shear, and dynamic clearance, controlled release of drugs is challenging. For example, as summarized in Table S1 (Supporting Information), most hydrogel systems rely on physical drug loading and exhibit burst release within days. [6,10,12-15,21] For hydrophobic drugs, NPs are typically used for encapsulation, [22] but this can lead to uncontrolled release of NPs, unwanted early-stage drug loss, and potential toxicity to surrounding ocular tissues.<sup>[2]</sup> These limitations in drug release kinetics, long-term retention, and formulation complexity, especially in the context of ocular physiology, underscore the need for an integrated strategy that addresses both functional performance and translational practicality. Building on our prior insights into NP-hydrogel integration, we aimed to develop a generalizable, biocompatible platform offering stable NP incorporation, strong wet tissue adhesion, and sustained drug release for ocular applications.

Here, we report a dynamic bridging strategy that leverages the multifunctional binding capacity of TA to physically tether drugloaded NPs within hydrogel matrices via hydrogen bonding. This approach stabilizes NP-hydrogel integration without requiring covalent modification. Building on our previously reported readyto-use hydrogel formulation, which was originally developed for hemostasis, soft tissue sealing, and optimized for toughness, adhesive properties, and long-term storage, [23] we adapted this system into a drug-eluting ocular patch, termed OcuTAPE. This new platform is semi-transparent, storage-stable, and rapidly adheres to the ocular surface with gentle pressing, allowing repeatable application and adjustment. OcuTAPE exhibits tissue-mimicking mechanics that improve comfort, durability, and wear resistance under ocular stress, addressing key limitations of existing ocular adhesives, including reliance on in situ gelation, limited repositionability, rapid drug release, and poor mechanical compliance. While the previously developed formulation served as a general sealant, its applicability in ocular tissues, repositioning capability, innate therapeutic efficacy, and drug delivery capabilities were not explored. Here, we leveraged TA not only as an adhesive moiety but also as a dynamic linker between the hydrogel and NPs, [24] enabling stable NP integration and controlled drug release. As a result, the final patch functions as a dual-purpose platform, capable of tissue sealing and sustained drug delivery, through a synthesis-free and multifunctional design. This approach overcomes limitations associated with conventional physical loading and may be broadly applicable to other nanocomposite hydrogel systems across diverse clinical settings. To demonstrate this concept, we used our previously optimized mPEG-b-p(HPMAm-Lac<sub>n</sub>) micelle (MC) formulation as a model nanocarrier, <sup>[25]</sup> to highlight TA's dual roles. Building upon our earlier findings, we also exploited the hydrogel's tissue-mimicking mechanics to enhance durability, wear resistance, and antioxidant capacity for improving therapeutic efficacy. We validated the physicochemical and therapeutic performance of OcuTAPE in vitro, ex vivo, and in vivo, including studies in rabbit and pig models. As a proof of concept, dexamethasone (Dex)-loaded MCs were used to treat intraocular inflammation. To demonstrate the versatility of our approach, we applied the TA-bridging strategy to a gelatin methacryloyl (GelMA)-TA hydrogel incorporating curcumin (Cur)-loaded poly (lactic-co-glycolic acid) (PLGA) NPs to investigate NP-hydrogel integration and potential for prolonged drug release. Together, these results establish TA bridging as a general and synthesis-free strategy for engineering drug-eluting nanocomposite hydrogels.

#### 2. Results

#### 2.1. Design and Characterization of OcuTAPE

We developed a ready-to-use, drug-eluting adhesive patch, named OcuTAPE, designed both to seal ocular injuries and to serve as a matrix for sustained drug delivery for the treatment of various ocular diseases. OcuTAPE was synthesized based on poly(ethylene glycol) diacrylate (PEGDA) hydrogel interpenetrated with *N*-Hydroxysuccinimide (NHS) conjugated alginate (Alg) and subsequently treated with TA/calcium (II) chloride (Ca<sup>2+</sup>) to achieve

.wiley.com/doi/10.1002/adfm.202516281 by University Of California, Los Angeles, Wiley Online Library on [22/08/2025]. See the Terms

on Wiley Online Library for rules of use; OA articles are governed by the applicable Creative Common

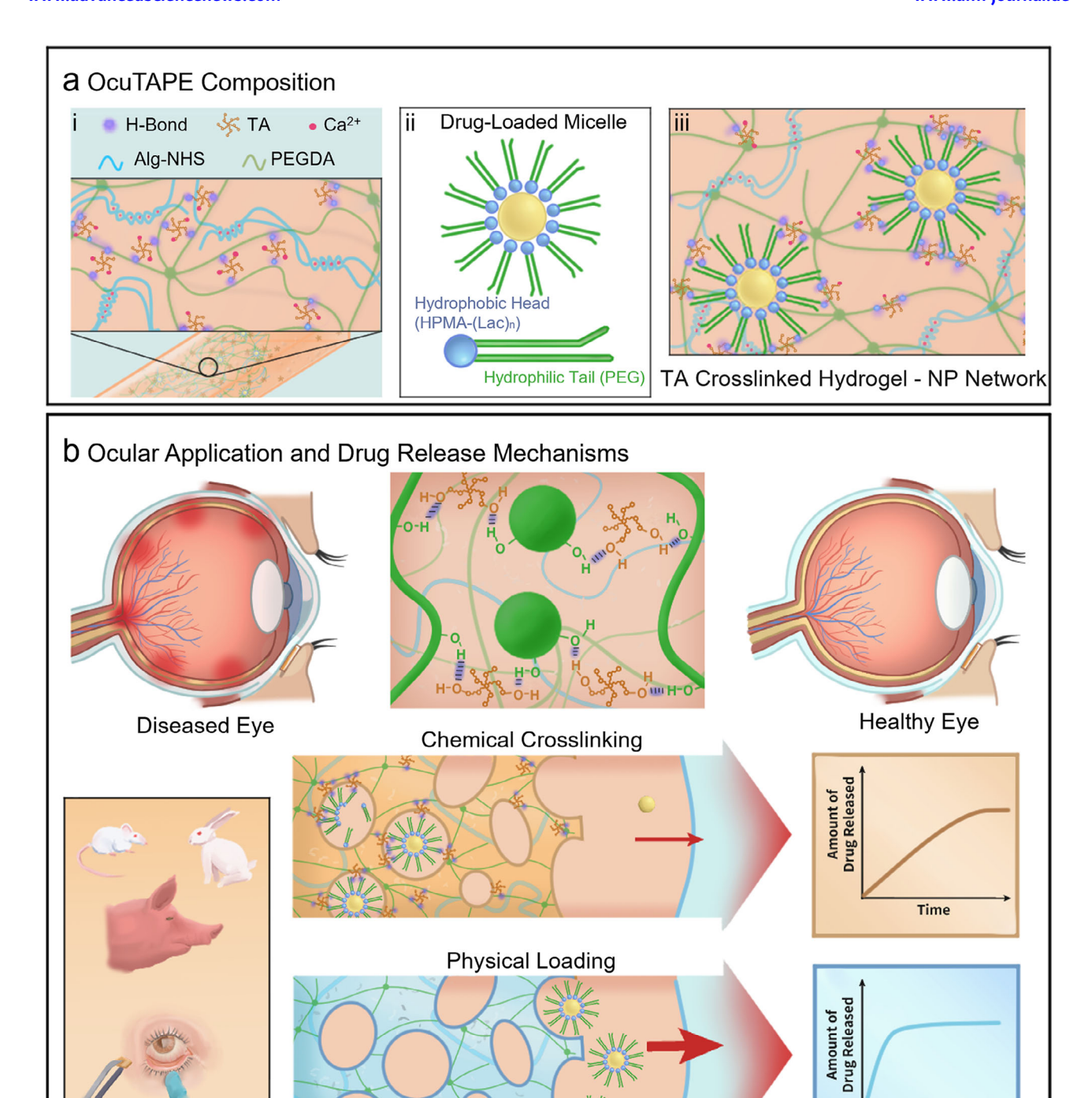


Figure 1. Schematic illustration of a) drug-loaded OcuTAPE composition and b) its application for treating ocular diseases with the drug release mechanisms.

tissue-mimicking and mucoadhesive properties (**Figure 1**ai). The goal of current drug delivery systems is to deliver active pharmaceutical ingredients (APIs) to target tissues with controlled release and effective local dosing.<sup>[26]</sup> In ophthalmic treatments, the frequent instillation of concentrated eyedrops is standard but faces limitations such as low bioavailability and reduced ther-

OcuTAPE Application

apeutic efficacy.<sup>[27]</sup> Many ocular medications, including corticosteroids and immunosuppressants, are hydrophobic,<sup>[28]</sup> which creates more challenges due to poor solubility and limited tissue permeability.<sup>[29]</sup> Drug-loaded nanocarriers have been designed to improve the bioavailability and pharmacokinetics of the encapsulated APIs, and to reduce their side effects.<sup>[30]</sup> In this study,

Time

1616282.6, Downloaded from https://advanced.onlinelbing.wiley.com/doi/10.1002/adfm.202516281 by University Of California, Los Angeles, Wiley Online Library on [22:08:2025]. See the Terms and Conditions (https://onlinelbitrary.viety.com/terms-and-conditions) on Wiley Online Library for rules of use; OA archies are governed by the applicable Centwise Commons I

we aim to develop MCs containing hydrophobic medications to treat ocular complications. MCs were formed through the self-assembly of amphiphilic polymers in an aqueous environment, allowing them to efficiently encapsulate hydrophobic drug molecules within their cores and improve the solubility of these medications (Figure 1aii). The combination of hydrogels with nanomaterials can be challenging, as most studies purely rely on physically loading the nanomaterials into the hydrogel.<sup>[25,31]</sup> This may imply the continuous release of NPs from the hydrogel into the external environment, leading to unwanted loss of medications during early release stages, and can cause a toxic effect to host tissues.[32] To overcome this obstacle, we adopted a strategy of efficiently crosslinking PEG-based MCs into a PEGbased hydrogel network using TA as a crosslinker, thereby preventing their leaching over time and improving release kinetics (Figure 1aiii). The formulated MC-loaded OcuTAPE is expected to provide sustained release kinetics (>5 weeks) as compared to physical loading. The optimized patch exhibits robust adherence to the conjunctiva, and the release of the drug occurs as a result of the degradation of the MCs through hydrolysis, leading to an improved therapeutic effect (Figure 1b). As a proof of concept, we loaded Dex to the OcuTAPE and demonstrated the effectiveness of the engineered platform in mitigating ocular inflammation.

The successful synthesis of PEGDA and Alg-NHS was confirmed with proton nuclear magnetic resonance (1H NMR) and Fourier-transform infrared (FTIR) spectroscopy based on the procedures explained in our previous work.[33] After the synthesis of PEGDA and Alg-NHS, the mixture of the two polymers (AP solution) was treated under visible blue light (405 nm) for 4 min in the presence of a lithium phenyl-2,4,6-trimethylbenzoylphosphinate (LAP) photoinitiator to form a covalently crosslinked PEGDA hydrogel network interpenetrated with Alg-NHS (AP hydrogel). The formed AP hydrogel was subsequently treated with TA/Ca<sup>2+</sup> to form OcuTAPE with improved and enhanced mechanical integrity and adhesive performance. The OcuTAPE patches were desiccated under vacuum at room temperature to remove excess surface moisture while retaining internal hydration. The goal was to achieve a semi-dry, flexible state suitable for handling and application. In our previous work, we developed a similar hydrogel system and molecular design strategy incorporating a TA/Fe<sup>3+</sup> complex, fully optimized as a general-purpose tissue adhesive with strong cohesive and adhesive properties. This formulation maintained stable adhesion performance after at least 6 months of vacuum-sealed storage at 4 °C.[33] Given its compositional similarity, OcuTAPE is expected to exhibit comparable long-term storage stability under the same conditions. In contrast, many commercial ocular adhesives, such as Histoacryl and TISSEEL, are supplied as single-use formulations with limited working time after opening.[34] TISSEEL additionally requires cold-chain storage, further restricting its usability in point-of-care settings.<sup>[35]</sup> Our previously developed platform was extensively optimized as a hemostatic sealant; however, the Fe<sup>3+</sup>-based formulation produced a dark black color, limiting its suitability for ocular applications. In the current study, we refined and adapted this hydrogel by eliminating the TA/Fe<sup>3+</sup> complex to develop a semi-transparent, ready-to-use ocular patch, designed to meet the unmet need for ocular adhesives that can both seal injuries and enable sustained therapeutic delivery.

We established the tunability of the mechanical properties of the engineered mucoadhesive patch by controlling a series of covalent and non-covalent interactions among Alg-NHS, PEGDA, TA, and Ca<sup>2+</sup> that collectively formed a multi-component macromolecular system. While the covalent network of PEGDA defined the primary backbone of the hydrogel, the reversible hydrogen bonding between PEGDA and TA, in addition to ionic interactions between Alg-NHS and Ca<sup>2+</sup>, together provided improved mechanical properties.<sup>[33]</sup> The chemical composition of OcuTAPE was verified using X-ray photoelectron spectroscopy (XPS), showing the presence of N and Ca elements in the hydrogel (Figure S1, Supporting Information).

As both Alg-NHS and TA can interact with Ca<sup>2+</sup> ions,<sup>[36]</sup> it is important to understand the effect of Alg-NHS and TA in their cross-interactions with Ca<sup>2+</sup>. Rheological studies were performed on Alg-NHS/Ca<sup>2+</sup> hydrogels and Alg-NHS/TA/Ca<sup>2+</sup> hydrogels, and the results were compared with those of the Alg/Ca<sup>2+</sup> and Alg/TA/Ca<sup>2+</sup> hydrogels (Figures S2,S3 and S4, Supporting Information). While native Alg with bare COOH groups formed a stronger hydrogel with Ca<sup>2+</sup> ions, the presence of NHS could tune the mechanical properties of the resulting hydrogel by reducing the "egg-box" crosslinking density (Figure S2, Supporting Information). Meanwhile, when Ca<sup>2+</sup> was chelated with TA, it still interacted with Alg or Alg-NHS to form a weak hydrogel. This was confirmed upon observing a greater elastic modulus (G') than the viscous modulus (G"). However, the G' and G" were lower in the hydrogels containing TA, particularly under frequency sweep conditions, compared to those without TA (Figure S3, Supporting Information). We also observed that native Alg with bare COOH groups formed a stronger hydrogel with TA/Ca<sup>2+</sup> as compared with Alg-NHS (Figure S4, Supporting Information). Therefore, we hypothesized that both TA and Alg-NHS may compete to interact with Ca<sup>2+</sup>. Overall, by introducing NHS and TA into the Alg/Ca<sup>2+</sup> network, the molecular interactions and crosslinking densities across the hydrogels were manipulated to tune their mechanical properties.[33] These rheological results confirm a crosslinking mechanism consistent with our previous findings involving the TA/Fe3+ complex in modulating the PEGDA/Alg-NHS network,[33] supporting the use of Ca<sup>2+</sup> as a biocompatible alternative. While detailed re-optimization was not the focus of this study, the observed gelation behavior and mechanical properties suggest that the formulation remains functional without obvious need for major adjustment to TA or Ca<sup>2+</sup> concentrations.

Since Alg-NHS can crosslink with Ca<sup>2+</sup> to form a dynamic ionic crosslinked network, the stiffness of OcuTAPE was tuned to match the native porcine conjunctiva tissue (95.2 ± 37.9 kPa) by varying the Alg concentrations to modulate crosslinking densities, <sup>[33]</sup> thereby minimizing inflammation caused by mechanical mismatch (**Figure 2a**). It was observed that by incorporating multimode crosslinking mechanisms, mechanical properties could be improved significantly. Additionally, adjusting the concentration of Alg-NHS allowed for the modification of the toughness of OcuTAPE. The toughness was enhanced by over 2-fold through the addition of Alg-NHS, exceeding 4000 kJ m<sup>-3</sup>. However, continued addition of Alg-NHS resulted in a decrease in toughness, likely attributed to the formation of a more rigid Alg-NHS/Ca<sup>2+</sup> crosslinked network, limiting the OcuTAPE's stretchability (Figure 2b). Therefore, we chose 22% PEGDA and

16163028, 0, Downloaded from https://advanced.

onlinelibrary.wiley.com/doi/10.1002/adfm.202516281 by University Of California, Los Angeles, Wiley Online Library on [22/08/2025]. See the Terms

and Conditions (https://onlinelibrary.wiley.com/term

und-conditions) on Wiley Online Library for rules of use; OA articles are governed by the applicable Creative Commons

www.afm-journal.de

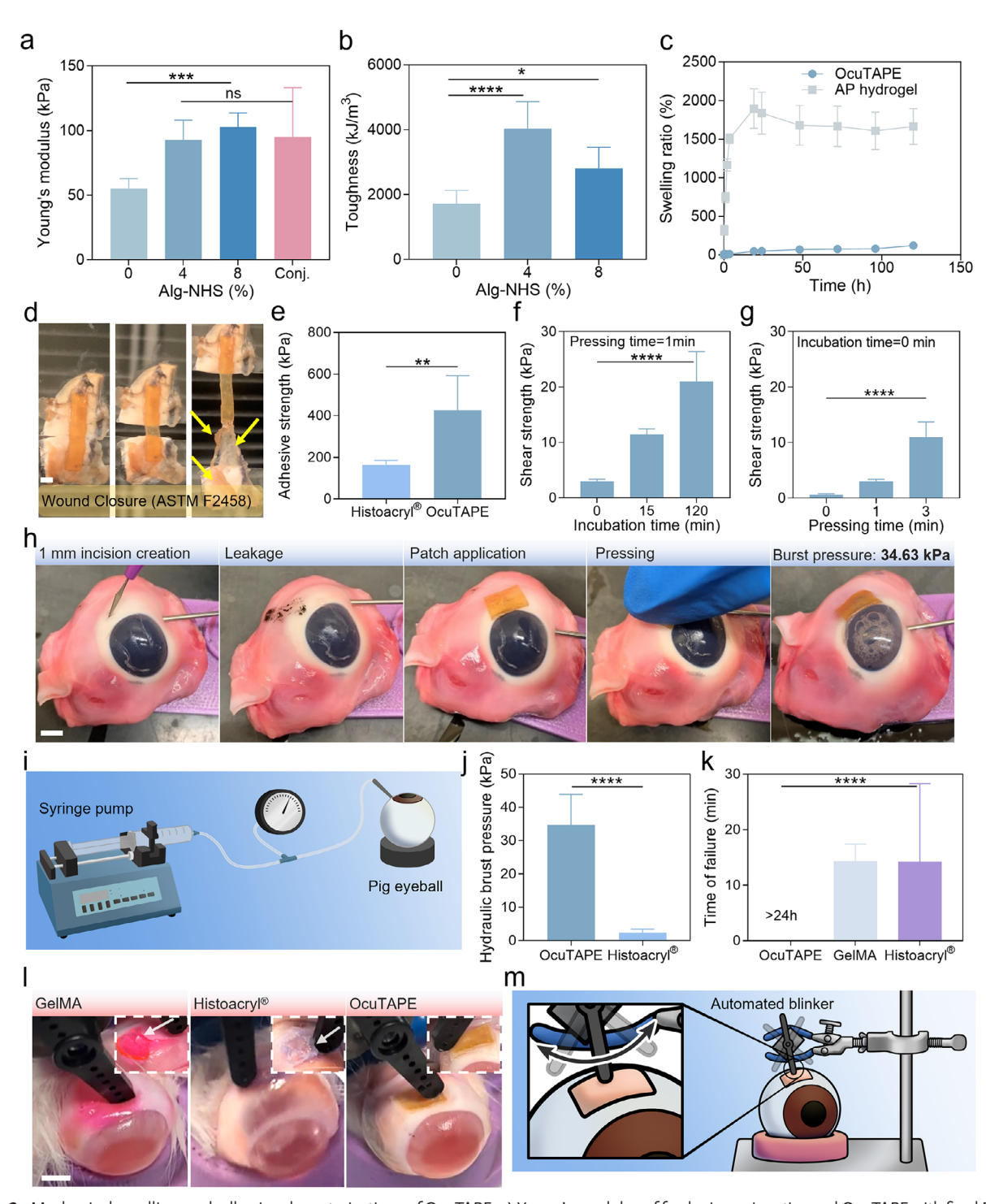


Figure 2. Mechanical, swelling, and adhesive characterizations of OcuTAPE. a) Young's modulus of fresh pig conjunctiva and OcuTAPE with fixed PEGDA concentration (22%) and varied Alg-NHS concentrations (0, 4, 8%). b) Toughness of OcuTAPE formed with varied Alg-NHS concentrations (0, 4, 8%). c) Swelling profile of OcuTAPE with and without TA/Ca<sup>2+</sup> (AP hydrogel) crosslinking. d) ASTM wound closure test (ASTM F2458) visual illustration (scale bars = 3 mm). e) Adhesive strength of OcuTAPE in comparison with the commercial cyanoacrylate glue (Histoacryl) in a wound closure test. Shear strength of OcuTAPE using different f) incubation time and g) pressing time. h) Visual images of OcuTAPE ex vivo application on porcine eyeball (scale bars = 8 mm). i) Burst pressure measurement setup connected via a needle to the vitreous body of the eye. j) Burst pressure comparison of OcuTAPE with cyanoacrylate (Histoacryl) applied on the conjunctiva. k) Time of failures of OcuTAPE, cyanoacrylate (Histoacryl), and GelMA under an automated blinker that applied continuous back-and-forth shear forces to detach hydrogels from freshly isolated rabbit eyeballs and the l) visual images of OcuTAPE, GelMA, and Histoacryl on the eyeballs after experiencing continuous back-and-forth shear forces after 30 min (scale bars = 8 mm). m) Illustrated schematic for the setup. Data are presented as mean  $\pm$  SD. \*p < 0.05; \*\*p < 0.01; \*\*\*\*p < 0.001; \*\*\*\*\*p < 0.0001; ns = not significant (t-test or one-way ANOVA). n  $\geq$  3.

1616282.6, Downloaded from https://advanced.onlinelbing.wiley.com/doi/10.1002/adfm.202516281 by University Of California, Los Angeles, Wiley Online Library on [22:08:2025]. See the Terms and Conditions (https://onlinelbitrary.viety.com/terms-and-conditions) on Wiley Online Library for rules of use; OA archies are governed by the applicable Centwise Commons I

4% Alg-NHS along with TA/Ca<sup>2+</sup> treatment as our final composition. This high toughness ensures its mechanical durability when OcuTAPE is subjected to repetitive wear and tear during eye movements and blinking.

In addition to tissue-mimicking mechanical properties, selfrecovery and fatigue resistance are essential characteristics in designing adhesive ocular materials, which enable them to overcome repeated cyclic loads and maximize their lifetime on dynamic eye surfaces. In this regard, the resilience of the OcuTAPE was investigated through a cyclic loading-unloading compression test under wet conditions. The representative cyclic strain and stress curves in Figure \$5a (Supporting Information) demonstrate that the OcuTAPE could withstand and recover from a large strain of 50% even after 60 cycles of loading and unloading. The consistent hysteresis loops over 60 cycles, along with the negligible change in dissipated energy, indicate that the engineered hydrogel exhibited high resilience with minimal plastic deformation (Figure S5b, Supporting Information). This suggests that the hydrogel maintained elasticity, allowing it to resist repeated forces without undergoing permanent structural changes, making it durable under mechanical stress.

For ocular application, it is crucial to minimize swelling, as it can not only exert pressure on the adjacent ocular tissue, causing discomfort and potential tissue damage, but also contribute to a gradual deterioration of toughness and leaching of drugcontaining MCs over time.[37] In our preliminary study, the Ocu-TAPE exhibited minimal swelling (Figure 2c) due to its high crosslinking density and added hydrophobicity resulting from the incorporation of TA.[38] In contrast, the AP hydrogel without TA/Ca<sup>2+</sup> crosslinking demonstrated rapid swelling with more than 1000% expansion within 10 h. The substantial swelling observed in the AP hydrogel is primarily attributed to the high hydrophilicity and relatively low crosslinking density of PEGDA. The ethylene oxide chains in PEGDA readily absorb water, leading to rapid and extensive volumetric expansion.[38] In the absence of additional physical or ionic crosslinkers, the hydrogel network remained loosely structured, allowing significant water infiltration. In contrast, the addition of TA and Ca<sup>2+</sup> ions introduced dense secondary crosslinking via hydrogen bonding and ionic interactions, enhancing network cohesion and reducing free volume for water uptake. This combination also increased hydrophobic character and restricted swelling. As a result, the OcuTAPE hydrogel maintain mechanical stability and minimizes ocular discomfort.

#### 2.2. In Vitro/Ex Vivo Adhesive Characterization of OcuTAPE

Our designed mucoadhesive patch can form a variety of non-covalent interactions and covalent interactions, including hydrogen bonds (from TA and NHS), Schiff-base reaction (from TA), Michael-type addition (from TA), and amidation (from NHS) with the active moieties on the ocular tissue/mucosal surface. [39] NHS and TA synergistically promote rapid adhesion to the eye. [33] Li et al. first demonstrated TA as a primer that enhanced hydrogel adhesion to ocular tissue through hydrogen bonding and hydrophobic interactions. [6] Our data demonstrated robust adhesion of OcuTAPE to porcine conjunctiva tissue in both the lap shear test (ASTM F2255) and wound closure test (ASTM F2458) with an ad-

hesive strength of 11.5  $\pm$  0.1 and 427.3  $\pm$  165.3 kPa, respectively (Figure S6a, Supporting Information). The shear strength of Ocu-TAPE was comparable to one of the strongest commercial bloadhesives, Histoacryl (n-butyl-2-cyanoacrylate), [40] as demonstrated in the lap shear test (Figure S6b, Supporting Information). The visual illustration of OcuTAPE in a lap shear test is demonstrated in Figure S6c (Supporting Information), where the patch remained adhered to the conjunctival tissue during the measurement, as indicated by the yellow arrows. However, OcuTAPE exhibited significantly higher performance in wound closure tests, potentially attributed to the cohesive failure observed with Histoacryl (Figure 2d,e). Additionally, OcuTAPE's adhesion to the conjunctiva was tunable by adjusting pressing time to the tissue and incubation time at 37 °C. When increasing pressing time (from 0 to 3 min) and incubation time (from 0 to 120 min), adhesion to the conjunctiva increased correspondingly (Figure 2f,g). This not only indicates the long-term adhesive properties of this patch but also gives clinicians a chance to do multiple readjustments while applying OcuTAPE by controlling the pressing duration. Commercial adhesives such as Evicel, [41] Coseal, [42] DuraSeal, [43] Histoacryl, [34,44] and TISSEEL[35,45] polymerize rapidly in situ and are supplied in sealed kits designed for single use. Once applied, they cannot be repositioned or reused. In contrast, Ocu-TAPE demonstrated repeatable application without compromising adhesive performance, as shown in Figure S6d (Supporting Information). The hydrogel exhibited consistent shear adhesive strength (≈2–3 kPa) after 1 min of pressing and immediate testing, even after 11 consecutiveapplications of attachment and detachment. While NHS esters can form covalent bonds with primary amines on tissue proteins, in our system, repeatable adhesion is primarily mediated by rapid, non-covalent interactions such as hydrogen bonding and hydrophobic interactions provided by TA,[6,38] especially during short contact time ( $\leq 1$  min). This is supported by the consistent shear adhesive strength observed over 11 rapid application cycles, indicating minimal contribution from progressive covalent bonding. Although NHSamine reactions can proceed faster under optimized conditions, they are generally more efficient at mildly basic pH (7.5-8.5) and longer contact durations.[46] However, the conjunctival surface presents a moist, mucin-rich environment with near-neutral pH  $(\approx 7.0-7.2)$ , [47] limited amine accessibility, and fast hydrolysis of NHS esters, which together suppress covalent bonding during brief contact times. Therefore, their role is likely limited during brief reapplication events. Our findings are consistent with previous studies demonstrating that non-covalent interactions can facilitate strong yet transient wet tissue adhesion. For instance, Yuk et al. [48] reported that in a poly(acrylic acid)-based dry doublesided tape (DST) functionalized with NHS esters, initial adhesion to wet porcine skin was driven by hydrogen bonding and electrostatic interactions between carboxylic acid groups and tissue surfaces, achieving >500 J m<sup>-2</sup> interfacial toughness and >80 kPa shear and tensile strength immediately after applying gentle pressure for a few seconds, even without NHS esters. However, the adhesion performance started to decline after ≈15 min in wet environments, highlighting the transient nature of non-covalent bonds. Notably, the NHS-containing DST achieved >710 J m<sup>-2</sup> interfacial toughness and >120 kPa shear and tensile strength after 24 h of equilibration, underscoring the role of NHS-mediated covalent coupling in stabilizing adhesion over time. To further

1616280.8, D. Dowloaded from https://advanced.oninelbray.wiley.com/doi/10.1002/adfm.202316281 by University Of California, Los Angeles, Wiley Online Library on [22:08:2025], See the Terms and Conditions (https://onlinelibrary.wiley.com/terms-and-conditions) on Wiley Online Library for rules of use; OA articles are governed by the applicable Cerative Commons.

www.afm-journal.de

confirm this, we performed repeated adhesion testing using a control hydrogel without NHS functionalization and observed similar adhesive behavior (Figure S7, Supporting Information). This supports the conclusion that TA-driven interactions primarily govern the reversible wet tissue adhesion. While NHS-amine reactions require relatively longer contact times to form stable covalent bonds, their inclusion allows for additional covalent reinforcement under conditions where extended contact is applied. Moreover, in real-world applications, such repeated adhesion is intended for short-term repositioning during initial placement rather than long-term reuse, further minimizing the likelihood of cumulative covalent bonding or nonspecific protein conjugation that could raise immunogenic concerns.

To further evaluate the adhesive properties of the engineered OcuTAPE, we utilized an ex vivo pig model using freshly explanted porcine eyes. In this experiment, we first created a 1 mm incision at the conjunctiva to induce a leakage, then OcuTAPE was applied to the incision site, followed by pressing for 1 min (Figure 2h). We then measured the hydraulic burst pressure using our custom-designed apparatus (Figure 2i). The results showed a conjunctival burst pressure of  $\approx\!34.6$  kPa ( $\approx\!260$  mmHg), which was significantly higher than the values obtained for cyanoacrylate ( $\approx\!2.3$  kPa), which could be due to the inherent wet tissue incompatibility of cyanoacrylate (Figure 2j; Video S1, Supporting Information). [49] Overall, the OcuTAPE exhibited favorable adhesive characteristics, enabling stable retention over the conjunctiva to facilitate the sustained release of the drug.

It's crucial to ensure that the adhesive hydrogel used as an ocular patch not only adheres well to wet surfaces but also maintains its integrity under mechanical forces like blinking. Blinking introduces repeated shear and tensile forces that can cause detachment or damage, even if the hydrogel initially adheres well. For example, the Li group reported that although certain hydrogel formulations initially adhered successfully to the ocular surface, they still suffered detachment or structural damage due to blinking stress over time. [6] To assess this, we conducted an experiment using an automated device that applied continuous back-and-forth shear forces to detach OcuTAPE from the freshly isolated rabbit eyeballs (Figure 2m) under wet conditions. Commercial Histoacryl and an in situ photocrosslinkable GelMA bioadhesive, were used as controls. The results revealed that both GelMA and Histoacryl exhibited cohesive and adhesive failures after ≈20 min of blinking, whereas OcuTAPE maintained robust adhesion and remained intact for over 24 h. (Figure 2k,l; Video S2, Supporting Information). These findings underscore the superior adhesive and cohesive properties of OcuTAPE, making it a promising candidate for ocular applications.

### 2.3. Engineering Drug-Loaded OcuTAPE and In Vitro Characterization

To show the efficacy of OcuTAPE for effective delivery of hydrophobic drugs, we engineered MCs using the procedures explained in our previous work with a slight modification. We then load two model drugs, Dex and Latanoprost (LP), inside these MCs prior to their incorporation within the OcuTAPE. Both

Dex and LP are widely used in clinical settings for treating intraocular inflammation and glaucoma, respectively.<sup>[50]</sup>

To date, existing drug-eluting ocular bioadhesives have relied solely on physical mixing for APIs delivery (Table S1, Supporting Information), which can lead to early-stage drug loss and potential toxicity to surrounding tissues. To overcome this challenge, we have implemented a strategy by effectively crosslinking the drug-loaded MCs into the hydrogel network using naturally derived polyphenols, preventing them from leaching out over time and improving the release kinetics. First, we synthesized biodegradable amphiphilic block copolymers of polyethylene glycol-b-(N-(2-hydroxypropyl) methacrylamide-co-oligolactate), [mPEG-b-p(HPMAm-Lac<sub>n</sub>)] via radical polymerization using (polyethylene glycol)<sub>2</sub>-4,4-azobis (4cyanopentanoic acid) (mPEG2-ABCPA) as a macroinitiator and N-(2-hydroxypropyl) methacrylamide-co-oligolactate (HPMAm-Lac,) as a monomer (ratio of monomer/initiator 150:1 mol mol<sup>-1</sup>) based on our previously published work.<sup>[25]</sup> The synthesized copolymer was then used to form MCs. The representative transmission electron microscopy (TEM) image of the MCs is shown in Figure 3a. Dex and LP were then separately loaded into the engineered MCs, resulting in formation of drug-loaded MCs with a narrow size distribution (polydispersity index (PDI) < 0.2) and an average size of  $\approx$ 100 nm, as confirmed by dynamic light scattering (DLS) (Figure 3b,c). The zeta potential of the MCs was close to 0 mV (Figure 3d), measured using a Zetasizer. The size discrepancy between DLS and TEM could be attributed to the hydrophilic PEG shell of the MCs, which retained a significant amount of water in solution. This water was lost during the drying process for TEM, resulting in the smaller size observed in the dried micellar structures.[51]

The loading efficiency of Dex and LP inside the engineered MCs was measured at around 34.8  $\pm$  3.8% and 62.9  $\pm$  0.9% at a 10:1 polymer/drug ratio based on a calibration curve obtained by high-performance liquid chromatography (HPLC), respectively (Figure 3e). We then formed OcuTAPE containing Dex or LPMCs by immersing the pre-formed hydrogel patch into a highly concentrated drug-loaded MCs solution (10% w v $^{-1}$ ) for 90 min, followed by washing with DI water to remove uncrosslinked MCs. The loading efficiency of the MCs within the OcuTAPE was found to be 30.4  $\pm$  10.5% for Dex and 24.6  $\pm$  1.5% for LP using HPLC (Figure 3f).

As the MC's hydrophilic tails consist of PEG, which has a strong affinity toward the TA in OcuTAPE through H-bonding interactions, [38] the MCs can be effectively crosslinked within the hydrogel network. The amount of the MCs crosslinked inside the hydrogel can be controlled by the size of the patch and potentially the crosslinking time, therefore, the dosage can be adjusted according to the patients' needs. To study the effect of MC crosslinking into OcuTAPE, we studied the release profile of Dex. To ensure accurate kinetic analysis, drug release studies were conducted under in vitro sink conditions using 50 mL of artificial tear fluid, [52] which prevents drug saturation, re-precipitation, or back-diffusion, especially critical given Dex's low aqueous solubility.[53] While this setup does not replicate the limited tear volume in vivo, it may approximate the effect of continuous tear turnover, reported to be approximately 10%-30% per minute in healthy individuals,[54] which facilitates drug clearance and reduces the likelihood of local saturation at the ocular surface. As

16163028, 0, Downloaded from https

onlinelibrary.wiley.com/doi/10.1002/adfm.202516281 by University Of California, Los Angeles, Wiley Online Library on [22/08/2025]. See the Terms

and-conditions) on Wiley Online Library for rules of use; OA articles are governed by the applicable Creative Commons

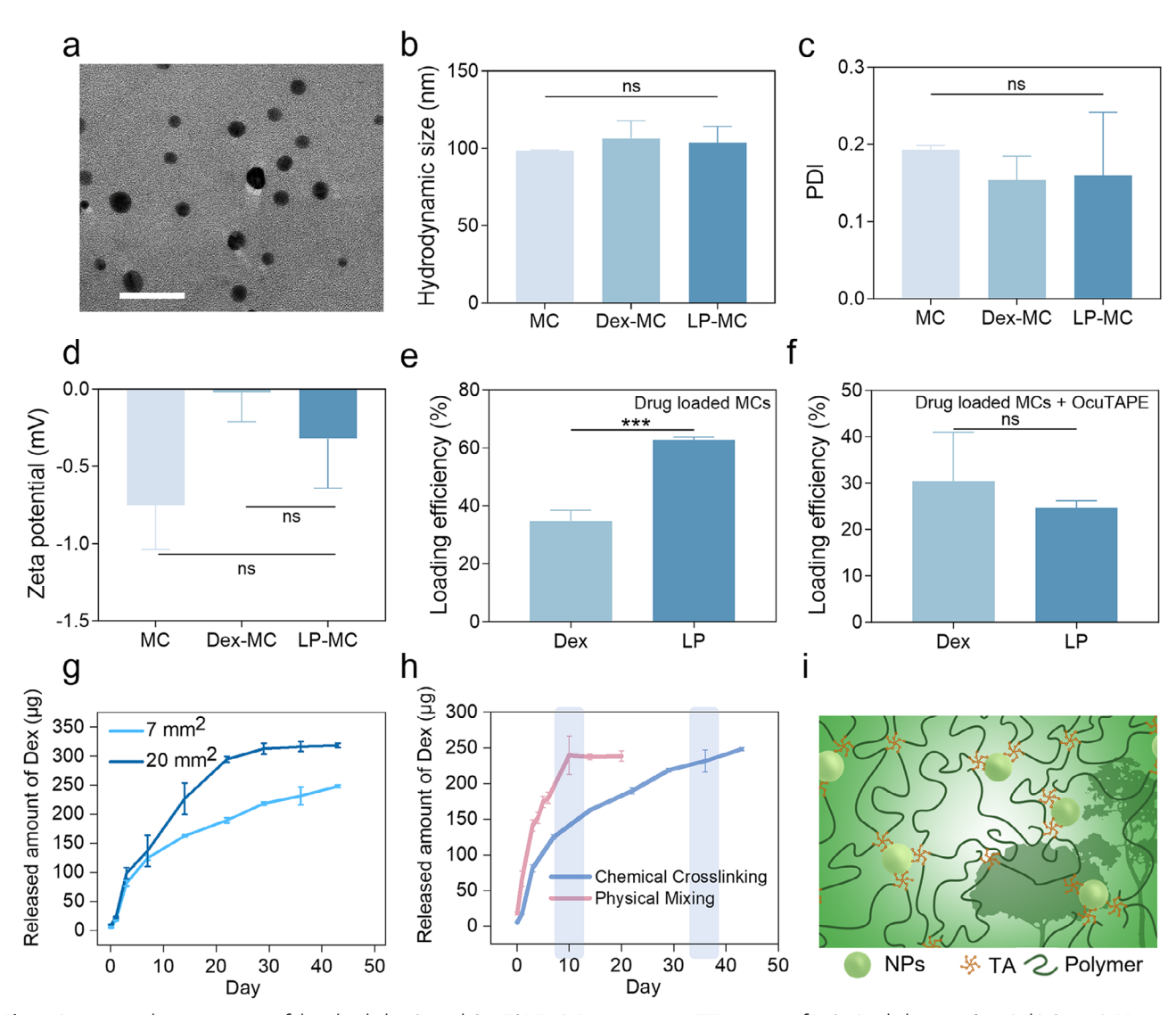


Figure 3. In vitro characterization of drug-loaded MCs and OcuTAPE. a) Representative TEM image of MCs (scale bars = 40 nm). b) Size, c) PDI, and d) zeta potential of LP-MC, Dex-MC, and drug-free MC. e) Loading efficiency of Dex and LP inside the MCs (10:1 polymer/drug). f) Loading efficiency of Dex-MC and LP-MC inside the OcuTAPE. g) The released amount of Dex from OcuTAPE. h) Released amount of Dex from OcuTAPE (with TA crosslinking) and AP hydrogel (without TA crosslinking). i) Illustration of TA's role as a crosslinking bridge. Data are presented as mean  $\pm$  SD. \*\*\* p < 0.001; ns = not significant (t-test or one-way ANOVA).  $n \ge 3$ .

shown in Figure 3g,  $248.2 \pm 2.3 \,\mu g$  and  $318.5 \pm 3.7 \,\mu g$  of Dex were slowly released over 5 weeks from the OcuTAPE with an area size of 7 mm² (5 mg in weight) and 20 mm² (15 mg in weight), respectively. To validate the efficacy of the TA-crosslinked MC-hydrogel network (chemically crosslinking) in enhancing the releasing profile, we also loaded Dex-MC directly into the AP hydrogel without TA crosslinking (physically mixing) and conducted a release experiment. As depicted in Figure 3h and Figure S8a,b (Supporting Information), all the drug compounds (100%) were released within 10 days for the physically mixed group, underscoring the crucial role played by TA in controlling the leaching of nanomaterials over time.

To evaluate MC stability under physiologically relevant ocular conditions, we conducted drug release studies at pH 7.4 (normal tears) and pH 6.5 (inflamed ocular environment). No significant

differences were observed between the two conditions in the free MC group (Figure \$9a,b, Supporting Information), indicating that the slightly acidic environment did not accelerate hydrolysis of the MCs. [55] However, when MCs were crosslinked within the OcuTAPE hydrogel, drug release was significantly slower than that of free MCs. This is likely due to multiple effects: i) TAmediated bridging formed hydrogen bonds with both the PEG shell and the surrounding hydrogel matrix, physically restricting MC diffusion and suppressing burst release; [56] ii) the reduced mobility within the hydrogel delayed water penetration and core disassembly, further slowing drug release; [25] and iii) TA may also form secondary interactions, such as hydrogen bonding or hydrophobic interactions, with Dex, reducing its diffusion. [57] Together, these mechanisms could contribute to the observed sustained release profile in OcuTAPE.

1616908, 0, Downbaded from https://advanced.onlinelibrary.wiley.com/doi/10.1002/adfm.202516281 by University Of California, Los Angeles, Wiley Online Library on [22082025]. See the Terms and Conditions (https://onlinelibrary.wiley.com/tems-and-conditions) on Wiley Online Library for rules of use; OA aricles are governed by the applicable Ceravive Commons

To quantitatively analyze the release kinetics of Dex from Ocu-TAPE, we fitted the experimental release profiles using three mathematical models commonly applied to NP-hydrogel systems: Korsmeyer-Peppas, Higuchi, and Weibull models. Among them, the Weibull model, [58] expressed as:  $F(t) = 1 - e^{-\alpha t^{\beta}}$ , showed the best fit for both physically loaded and chemically crosslinked systems, with coefficients of determination (R2) exceeding 0.99, indicating strong predictive accuracy (Figure \$10, Supporting Information).  $\alpha$  is the rate constant,  $\beta$  is the shape parameter, and F(t) is the released proportion at time t. This model accounts for both time-dependent diffusional transport and structural constraints within the matrix, making it wellsuited for describing heterogeneous systems such as nanocomposite hydrogels. [59] The physically loaded system exhibited a relatively high  $\alpha$  and lower  $\beta$ , characteristic of faster, diffusiondriven release with limited structural hindrance.<sup>[59]</sup> In contrast, TA-mediated chemical crosslinking of PEG-based MCs within OcuTAPE significantly decreased  $\alpha$  and increased  $\beta$ , reflecting a delayed onset and more sigmoidal release profile. [59] This shift suggests a transition from Fickian diffusion to anomalous transport, driven by strong, reversible hydrogen bonding between TA and PEG domains within both the MCs and the hydrogel network. These interactions create a dynamic yet physically restrictive environment, impeding MC diffusion and slowing drug liberation. Furthermore, the higher  $\beta$  value in the crosslinked system implies a more controlled and coordinated release process, where drug transport is governed not only by concentration gradients but also by structural relaxation and microenvironmental resistance. [60] This behavior highlights the dual functionality of TA by not only enhancing adhesive and mechanical properties, but also serving as a dynamic bridging agent that regulates NP mobility and modulates drug release kinetics. This strategy enables fine-tuning of release rates through reversible, non-covalent interactions without the need for chemical modification.

Due to its five-arm chemical structure and abundance of phenolic hydroxyl groups capable of forming hydrogen bonds, [61] TA can provide a potential platform for crosslinking of various NPs within hydrogel matrices. This is feasible if both the NPs and the hydrogel prepolymers possess hydrogen bonding sites that can interact with TA. A wide range of biopolymers commonly used in drug delivery, tissue engineering, and coatings have shown a strong affinity for TA, including polyvinyl alcohol (PVA), [62] gelatin, [39] polyvinylpyrrolidone (PVP), [39] and polyacrylamide (PAM),[63] polyacrylic acid[64] and many others (Figure 3i). To visually show the impact of TA crosslinking on controlled release of drugs, the engineered MCs were loaded with the hydrophobic dye Oil Red O. A TA-crosslinked PEGDA hydrogel was then soaked in the MCs solution for 5 min, with noncrosslinked PEGDA hydrogel serving as a control. After soaking, both hydrogels were thoroughly washed under flowing Milli-Q water. As shown in Figure S11a (Supporting Information), the TA-crosslinked hydrogel effectively retained the MCs containing dye Oil Red O, whereas the pure PEGDA hydrogel without TA crosslinking did not. This result suggests that hydrogen bonding occurred between the TA in the hydrogel and the PEG units of the MCs, enabling the retention of MCs in the crosslinked hydrogel. To demonstrate the effectiveness of this strategy compared to conventional physical encapsulation, dye-loaded MCs were physically encapsulated into a 7% (w/v) GelMA bioadhesive

following our previously published protocol for creating in situ photocrosslinkable drug-eluting ocular adhesives.<sup>[25]</sup> The MCsloaded GelMA hydrogels were then placed in Dulbecco's Phosphate Buffered Saline (DPBS), and the leaching of MCs was compared to that from the TA crosslinked PEGDA hydrogel. As shown in Figure S11b (Supporting Information), the MCs leached out from the GelMA hydrogel within 2 h, while the MCs remained stably encapsulated in the TA-crosslinked hydrogel for over 10 days without significant leaching. This stark difference underscores the effectiveness of the hydrogen bonding between TA and the PEG units of the MCs and hydrogel, which allows for sustained retention and release control, making the system a more robust option for long-term drug delivery applications compared to the traditional encapsulation method.

#### 2.4. In Vitro and In Vivo Biocompatibility of OcuTAPE

The biocompatibility of OcuTAPE was evaluated through in vitro cytotoxicity assessments using NIH 3T3 cells. As shown in Figure 4a, OcuTAPE effectively supported the viability and attachment of 3T3 cells, showing no discernible difference compared to the control group, where the cells were cultured in a 24 well-plate with no treatment. Additionally, quantitative analysis revealed a consistently high level of cell viability (>95%) over a 7-day culture period (Figure 4b; Figure S12a, Supporting Information), providing further evidence of the non-cytotoxic nature of OcuTAPE. Fluorescent staining using Alexa Fluor 488 phalloidin and DAPI confirmed cell spreading on OcuTAPE over the 7-day culture period, similar to the control group (Figure 4c; Figure S12b, Supporting Information). Cell proliferation was also assessed with PrestoBlue, a resazurin-based cell viability reagent, which demonstrated an increase in metabolic activity of 3T3 cells over 7 days for both OcuTAPE and the control, as depicted in Figure 4d. These collective findings affirm the in vitro biocompatibility of OcuTAPE.

Next, we evaluated the biocompatibility of the OcuTAPE in vivo through subcutaneous implantation in the dorsal connective tissue of Wistar rats (Figure 4e). This widely established small animal model is ideal for assessing biomaterial biocompatibility due to its cost-effectiveness, ease of handling, and ability to generate reproducible results. Findings from this model can be effectively extrapolated to larger animal studies and potential clinical applications. [65] As indicated by the yellow arrows in Figure 4f,g, Hematoxylin and eosin (H&E), and Masson's trichrome (MT) staining confirmed cell infiltration around the tissue-hydrogel interface at both day 7 and day 14. MT staining showed no obvious collagen deposition at the hydrogel-tissue interface, indicating no significant fibrosis. These findings confirm the biocompatible nature of the engineered hydrogel, showcasing its ability to integrate with host tissues. The inflammatory phase, the second stage of wound healing, commences with the infiltration of neutrophils and macrophages. [66] Immunohistochemistry (IHC) staining of immune cells (CD68 and CD3) was conducted to evaluate the local immune response. Macrophage invasion at the hydrogel-subcutaneous tissue interface was observed on day 7, likely in response to the host tissue, but disappeared by day 14 post-surgery (Figure 4h; Figure S13, Supporting Information). This observation further indicates the in vivo biocompatibility of

16163028, 0, Downloaded from https://advanced

onlinelibrary.wiley.com/doi/10.1002/adfm.202516281 by University Of California, Los Angeles, Wiley Online Library on [22/08/2025]. See the Terms

and Conditions (https://onlinelibrary.wiley.com/term

and-conditions) on Wiley Online Library for rules of use; OA articles are governed by the applicable Creative Commons

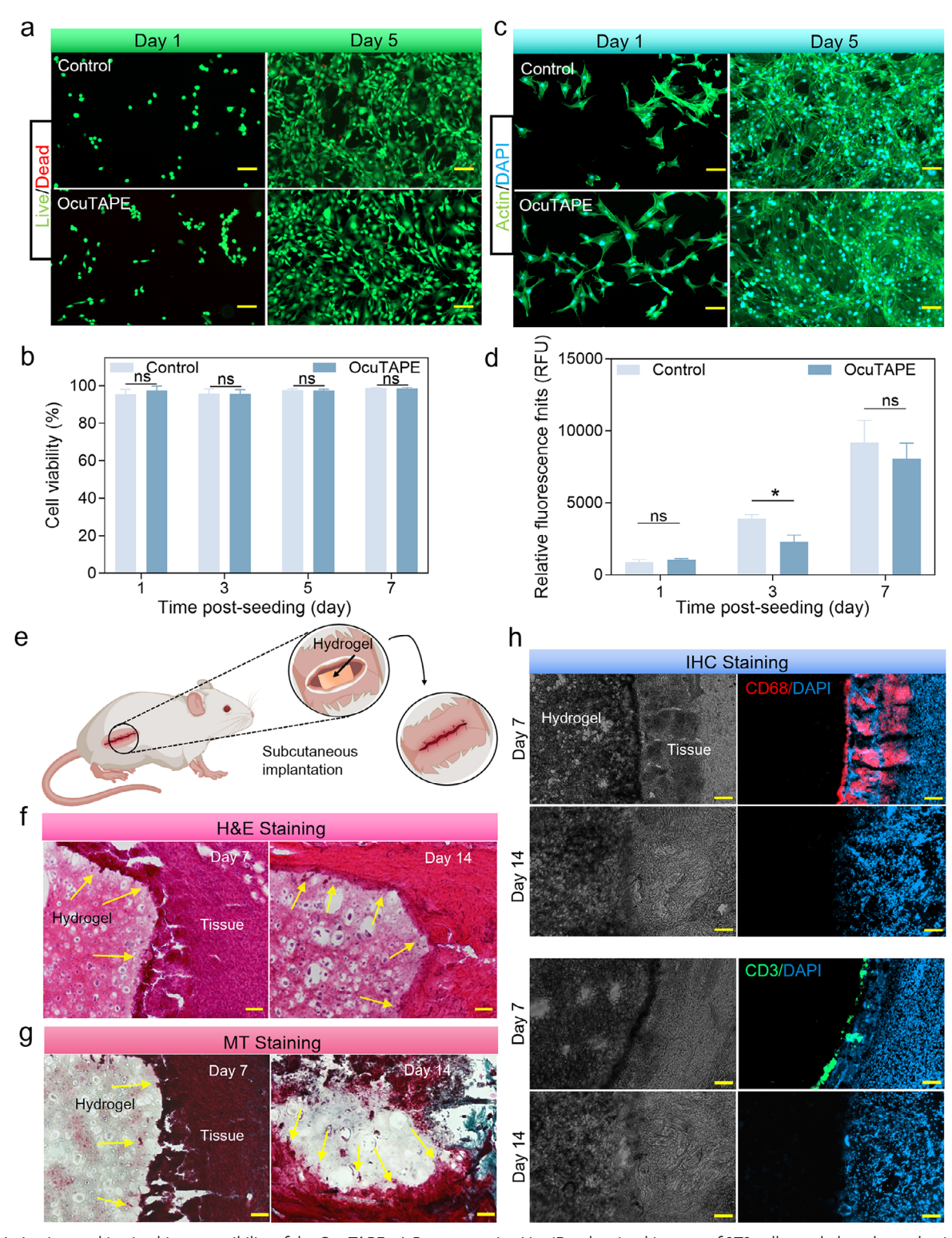


Figure 4. In vitro and in vivo biocompatibility of the OcuTAPE. a) Representative Live/Dead stained images of 3T3 cells seeded on the underside of the Transwell permeable supports with OcuTAPE or without treatment, at 1- and 5-days post-seeding (scale bars =  $100 \, \mu m$ ). b) Quantification of cellular viability over 7 days of culture. c) Representative F-actin/DAPI stained images of 3T3 cells seeded on the underside of the Transwell permeable supports with OcuTAPE hydrogels or without treatment, at 1- and 5-days post-seeding (scale bars =  $100 \, \mu m$ ). d) Quantitative analysis of cellular metabolic activity, shown as relative fluorescence units (RFU), for OcuTAPE at days 1, 3, and 7 post-seeding, compared to the no-treatment control group. e) Schematic demonstration of subcutaneous implantation of hydrogel in rats. f) H&E, g) MT, and h) IHC staining from the OcuTAPE/tissue interfaces at days 7 and 14 post-implantation (scale bars =  $100 \, \mu m$ ). Data are presented as mean  $\pm$  SD. \*p < 0.05; ns = not significant (two-way ANOVA). n  $\geq$  3. The schematic diagram was created using BioRender software (biorender.com).



1616280.8, D. Dowloaded from https://advanced.oninelbray.wiley.com/doi/10.1002/adfm.202316281 by University Of California, Los Angeles, Wiley Online Library on [22:08:2025], See the Terms and Conditions (https://onlinelibrary.wiley.com/terms-and-conditions) on Wiley Online Library for rules of use; OA articles are governed by the applicable Cerative Commons.

www.afm-journal.de

OcuTAPE, which is due to its biocompatible material compositions, including Alg, PEG, TA, and Ca<sup>2+</sup>.<sup>[23]</sup>

To the best of our knowledge, currently available ocular adhesives have shown limitations in simultaneously achieving strong tissue adhesion and comprehensive in vitro and in vivo biocompatibility. Many effective bioadhesives with strong mechanical properties and tissue adhesion, such as cyanoacrylates, have been associated with cytotoxic effects and inflammation.<sup>[23,67]</sup> Additionally, cyanoacrylate adhesives can cause tissue burns due to exothermic polymerization, possess stiffness that exceeds that of skin and other soft tissues,<sup>[68]</sup> and may not adapt well to the dynamic movements of the eye. In contrast, our engineered OcuTAPE offers enhanced adhesive strength compared to commercial bioadhesives, while ensuring biocompatibility.

### 2.5. In Vivo Ocular Retention and Biosafety of OcuTAPE in Large Animals

To further evaluate the biosafety and clinical translational potential of our engineered ocular bioadhesive, we employed a live pig model to assess immediate adhesion to ocular surfaces as well as a live rabbit model to study long-term adhesion and biosafety (up to two weeks) of the OcuTAPE. For the pig study, OcuTAPE was applied to the conjunctiva of the pig eyeball, and gentle pressure was applied for 1 min to promote adhesion. Following the application, the hydrogel demonstrated immediate and robust adhesion, which was further confirmed by attempting to remove it with a tweezer. This method allowed us to assess the adhesive strength and stability of OcuTAPE on ocular tissues under physiologically relevant conditions (Figure 5a; Video S3, Supporting Information). This result highlights OcuTAPE's potential for clinical translation and its ability to improve the management of ocular disorders.

Following confirmation of its immediate adhesion on the pig eves in vivo, we used a live rabbit model to further investigate the long-term retention and biosafety of OcuTAPE on the ocular surface. Following anesthesia, OcuTAPE was placed at the corneoscleral junction on the left eye by gently pressing the patch against the eyelids, as shown in schematic Figure 5b. Contralateral eyes (right eye) without any patch were used as controls. The retention and degradation of the patch overtime were confirmed by stereoscopic (Figure 5c) and optical coherence tomography (OCT) (Figure 5d) imaging, which confirmed the physical presence of OcuTAPE until day 14 without any adverse effect either on the ocular surface or the retina (we did not test beyond 14 days due to limitations on our protocol). Further, we investigated the effect of OcuTAPE on intraocular pressure (IOP) elevation, if any, and our data indicated that OcuTAPE did not cause an elevation in IOP (Figure 5e). We also evaluated the adverse effects of Ocu-TAPE by assessing the tissue damage and leukocyte infiltration in the corneal and retinal tissue by H&E staining. Our results indicated that OcuTAPE did not induce any noticeable leukocyte infiltration or disrupt the tissue architecture of the retina and cornea (Figure 5f). Together, our results suggest that OcuTAPE could provide better retention without any adverse effects on the ocular surface as well as the interior of the eye, and therefore can be used for sustained drug release to treat ocular diseases.

### 2.6. In Vitro and In Vivo Ocular Therapeutic Efficacy of Drug-Loaded OcuTAPE

To further demonstrate the drug-eluting property and therapeutic efficacy of our engineered drug-loaded OcuTAPE, we fabricated a formulation of Dex-OcuTAPE and tested in vitro using a Transwell migration assay, as shown in Figure 6a. Myeloid origin macrophages are infiltrating immune cells that play a key role in inflammation during ocular infectious and inflammatory diseases, [69] therefore we used bone marrow-derived macrophages (BMDM) to test the anti-inflammatory properties of Dex-loaded OcuTAPE in vitro. The mouse BMDM cells were seeded in the bottom well of a transwell plate and stimulated with lipopolysaccharide (LPS) for 24 h to induce the inflammatory response. The Dex-OcuTAPE was then placed on top of the insert membrane. The anti-inflammatory effect of Dex eluting from the OcuTAPE was assessed by measuring the mRNA transcripts of a few key inflammatory cytokines (e.g., IL-1 $\beta$ , IL-6) and chemokine (e.g., CCL2)<sup>[69,70]</sup> from BMDM cells using quantitative polymerase chain reaction (qPCR) analysis.

Our results showed that LPS stimulation induced an inflammatory cytokine/chemokine response, while Dex-OcuTAPE significantly attenuated this response in BMDM across all tested cytokines/chemokines, including IL-1 $\beta$ , IL-6, and CCL2 (Figure 6bi–iii). These findings confirm that the engineered OcuTAPE loaded with Dex could efficiently suppress the inflammatory response in vitro.

To further assess the therapeutic efficacy of Dex-loaded Ocu-TAPE, we used a mouse model of ocular inflammation. For this study, a blank OcuTAPE, a commercial Dex ophthalmic eye drop (0.1%, Bausch+Lomb), and Histoacryl were used as controls to compare the efficacy. Intraocular inflammation was induced in C57BL/6 wild-type (WT) mice eyes by a single intravitreal injection of LPS (100 ng/eye). Dex-loaded OcuTAPE, empty Ocu-TAPE, and Histoacryl were then placed on the corneoscleral surface (Figure 6c) immediately after the LPS injection in the treatment group. Dex ophthalmic eye drops were applied topically twice a day after the LPS injection. LPS-injected mice without any treatment were used as diseased animal controls, and mouse eyes with DPBS injection were used as mock controls. The neural retina was harvested 24 h post-treatment, and the level of pro-inflammatory cytokines was measured using qPCR analysis. The qPCR analysis revealed a significant reduction in LPSinduced pro-inflammatory mediators such as TNF- $\alpha$ , IL-1 $\beta$ , IL-6, CXCL-1, CXCL-2, CXCL-5, and CXCL-10 in Dex, blank Ocu-TAPE, and Dex-loaded OcuTAPE groups in comparison to untreated groups (Figure 6d-j). In contrast, Histoacryl did not show any anti-inflammatory effect and was comparable to the LPSinjected group. Its limited therapeutic efficacy may be attributed to a lack of bioactivity and suboptimal tissue integration. Additionally, its exothermic polymerization and potential release of cytotoxic byproducts such as formaldehyde<sup>[71]</sup> could contribute to local tissue stress.

Given the eye's immune-privileged nature, even transient or localized inflammation can lead to irreversible damage and vision loss. Pathogen-associated molecular patterns, such as LPS, peptidoglycan, and lipoteichoic acid, have been shown to initiate intraocular inflammation and tissue degeneration. [72] Although current therapies, such as topical eye drops or intraocular

16163028, 0, Downloaded from https://advanced.

onlinelibrary.wiley.com/doi/10.1002/adfm.202516281 by University Of California, Los Angeles, Wiley Online Library on [22/08/2025]. See the Terms

and Conditions (https://onlinelibrary.wiley.com/term

and-conditions) on Wiley Online Library for rules of use; OA articles are governed by the applicable Creative Commons

www.afm-journal.de

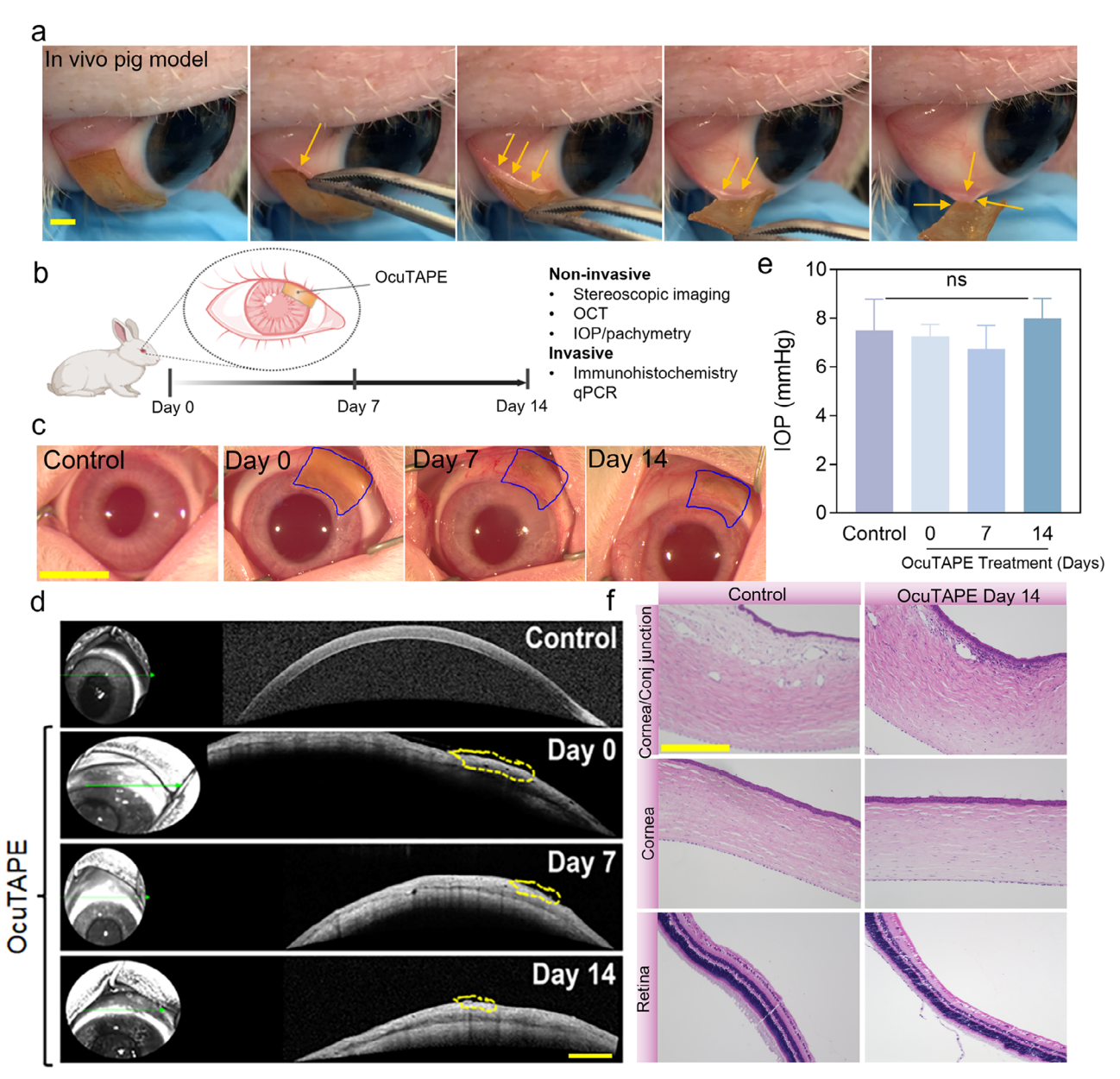


Figure 5. In vivo ocular retention, biosafety assessment of the OcuTAPE. a) Ocular adhesion assessment on a pig eye, showing firm attachment and retention of OcuTAPE on eye surface (scale bars = 5 mm). b) The schematic shows the placement of OcuTAPE on rabbit eyes, the timeline of the study, and downstream analysis for retention and safety evaluation. c) An empty OcuTAPE (without drug) was placed on the New Zealand White rabbit's eyes. The contralateral eyes without a patch were used as a control. The stereoscopic images show the retention of the OcuTAPE on days 0, 7, and 14 after placement (scale bars = 9 mm). d) OCT images show the positioning and retention of the OcuTAPE on the corneal-conjunctival junction (the dotted demarcation indicates the patch position) (scale bars =  $50 \mu m$ ). e) IOP was recorded on days 0, 7, and 14 after OcuTAPE placement using a Tonolab tonometer. No changes in IOP were noticed between the treated and control eyes. f) Eyes were enucleated at 14 days post-OcuTAPE placement and subjected to H&E staining. No noticeable leukocyte infiltration or tissue damage was observed in OcuTAPE-treated eyes compared to control eyes (scale bars =  $50 \mu m$ ). The bar graph represents the mean  $\pm$  SD of 3 rabbits/group. ns: not significant (one-way ANOVA). n = 3.

injections of choice of drugs, are widely used for ocular disease treatments, their efficacy is often compromised by limited retention, rapid clearance, and suboptimal drug penetration.<sup>[73]</sup> Ocular adhesive hydrogels have emerged as potential solutions to enhance local drug delivery; however, most existing adhesives serve merely as passive carriers without contributing therapeutic benefits.

Our TA-crosslinked OcuTAPE presents a multifunctional alternative that combines sustained drug delivery, bioadhesion, and therapeutic activity in a single platform. TA plays a central role not only in bridging the NP-hydrogel network but also in enhancing tissue adhesion. At the same time, TA imparts intrinsic antioxidant and anti-inflammatory properties, allowing blank OcuTAPE to actively suppress inflammation. This dual

16163028, 0, Downloaded from https://advanced

onlinelibrary.wiley.com/doi/10.1002/adfm.202516281 by University Of California, Los Angeles, Wiley Online Library on [2208/2025]. See the Terms

and Conditions (https://onlii

ons) on Wiley Online Library for rules of use; OA articles are governed by the applicable Creative Commons

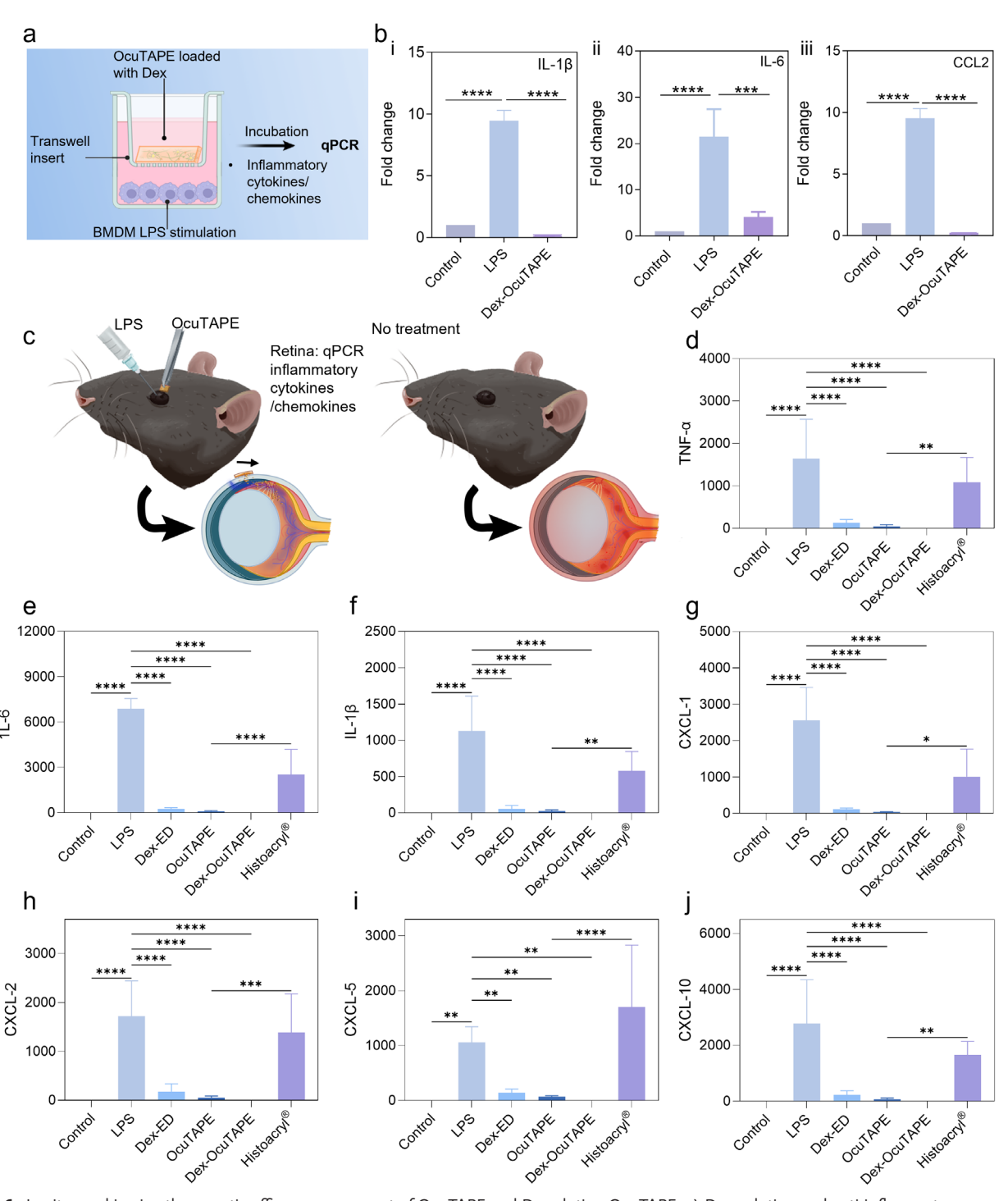


Figure 6. In vitro and in vivo therapeutic efficacy assessment of OcuTAPE and Dex-eluting OcuTAPE. a) Drug-eluting and anti-inflammatory properties of Dex-OcuTAPE were tested in vitro using a transwell migration assay. Bottom wells of 12-well transwell inserts were seeded with BMDM and stimulated with LPS (100 ng mL $^{-1}$ ). Dex-OcuTAPE (n = 4) were placed on the top of the insert, as shown in the schematic. BMDM with LPS stimulation was used as no treatment controls (LPS). Cells without LPS stimulation were used as mock controls. b) 24 h post-treatment, cells were harvested and subjected to qPCR analysis to measure the relative mRNA levels of i) IL-1 $\beta$ , ii) IL-6, and iii) CCL2 genes. c) Schematic showing placement of OcuTAPE on mouse eyes. The mice were intravitreally injected with LPS to induce intraocular inflammation, and blank OcuTAPE, Dex eye drops (Dex-ED), Dex-loaded OcuTAPE, and Histoacryl were applied at the corneoscleral junction. After 24 h of treatment, retinal tissue was harvested and subjected to qPCR analysis to measure the relative mRNA expressions of d) TNF- $\alpha$ , e) IL-6, f) IL-1 $\beta$ , g) CXCL-1, h) CXCL-2, i) CXCL-5, and j) CXCL-10 genes. The blank OcuTAPE, Dex, and Dexloaded OcuTAPE significantly reduced intraocular inflammation in comparison to LPS-injected and untreated eyes. The bar graph represents the mean  $\pm$  SD of six mice/group. \*p < 0.05; \*\*p < 0.01; \*\*\*\*p < 0.001; \*\*\*\*\*p < 0.0001; ns = not significant (one-way ANOVA). n = 6. The schematic diagram was created using BioRender software (biorender.com).



1616282.6, Downloaded from https://advanced.onlinelbing.wiley.com/doi/10.1002/adfm.202516281 by University Of California, Los Angeles, Wiley Online Library on [22:08:2025]. See the Terms and Conditions (https://onlinelbitrary.viety.com/terms-and-conditions) on Wiley Online Library for rules of use; OA archies are governed by the applicable Centwise Commons I

www.afm-journal.de

adhesive-therapeutic functionality is particularly advantageous in managing acute or moderate ocular inflammation, where a steroid-sparing approach may be desired to reduce side effects and broaden clinical applicability.

While blank OcuTAPE effectively suppressed acute inflammation, the incorporation of Dex remains important for addressing more severe or chronic inflammatory conditions. As our current model evaluates short-term responses, future studies will explore long-term and recurrent inflammation models to assess the added benefit of sustained Dex release. Additionally, we plan to evaluate the therapeutic utility of OcuTAPE in other chronic ocular diseases such as glaucoma. Having demonstrated successful encapsulation of LP, a prostaglandin analog widely used to lower intraocular pressure by enhancing uveoscleral outflow, we will next assess the in vivo efficacy of LP-loaded OcuTAPE in preclinical models of glaucoma. These studies will be essential to establish the platform's potential as a long-acting, non-invasive treatment option that addresses both disease management and patient compliance.

Together, the in vitro and in vivo data highlight the translational potential of our engineered platform as an effective therapeutic system for a broad range of ocular conditions, including uveitis, glaucoma, and ocular infections or inflammation.

### 2.7. In Vitro and In Vivo Reactive Oxygen Species (ROS)-Scavenging Effects of OcuTAPE

To further investigate the mechanism underlying the observed anti-inflammatory effects, we assessed oxidative stress markers at both the cellular and tissue levels. Free radicals on the ocular surface play a crucial role in normal cellular signaling and defense. However, when their production becomes excessive, the eye's antioxidant defenses can be overwhelmed, leading to oxidative stress.<sup>[74]</sup> This imbalance may result in damage to cellular components, triggering inflammation, tissue degeneration, and potentially compromising vision.<sup>[75]</sup> Prolonged oxidative stress is a key factor in the development of various ocular pathologies, including cataracts,<sup>[76]</sup> age-related macular degeneration,<sup>[77]</sup> dry eye,<sup>[78]</sup> and glaucoma,<sup>[79]</sup> underscoring the need for effective regulation of free radical activity to preserve ocular health.

TA is recognized for its effective radical-scavenging properties, attributed to its plentiful hydroxyl groups, making it a potential antioxidant for treating ocular diseases linked to high levels of ROS.[80] To investigate the antioxidant properties of the engineered OcuTAPE in vitro, we performed a DPPH• assay using 1,1-diphenyl-2-picrylhydrazine (DPPH•) as a stable free radical. Fresh DPPH osolutions were combined with Ocu-TAPE and the AP hydrogel, then incubated at room temperature for 5 min before analysis via UV-vis spectroscopy. A notable decrease in the absorbance peak at 517 nm, characteristic of DPPH•, was observed when mixed with OcuTAPE (Figure 7a; Figure \$14a, Supporting Information), confirming its substantial radical-scavenging capability. In comparison, the AP hydrogel showed minimal changes in absorbance, highlighting TA's importance in exhibiting antioxidant activity. We also calculated the percentage of DPPH• scavenging activity, demonstrating that OcuTAPE exhibited  $\approx$ 96.2  $\pm$  0.3% scavenging, while the AP hydrogel displayed only  $33.1 \pm 2.3\%$  scavenging (Figure 7b).

The ROS scavenging capability of OcuTAPE was further evaluated in vitro using the 2'-7' dichlorofluorescin diacetate (DCFH-DA) assay, where intracellular ROS levels are indicated by a green, fluorescent signal. [81] Cells exposed to hydrogen peroxide ( $H_2O_2$ ) displayed a significant increase in fluorescence, indicating elevated levels of ROS. However, the introduction of OcuTAPE resulted in a marked decrease in fluorescence intensity (Figure 7c), highlighting its effective ROS-scavenging properties. In contrast, the AP hydrogel, which lacks TA incorporation, exhibited minimal antioxidant activity (Figure 7c,d), further emphasizing the significant antioxidant effects attributed to TA.

In the LPS-induced mouse model of intraocular inflammation, qPCR analysis of neural retinal tissue showed that treatment with blank OcuTAPE, Dex-loaded OcuTAPE, and free Dex significantly reduced the expression of inducible nitric oxide synthase (NOS2) and NADPH oxidase 4 (NOX4), two enzymes associated with pathological ROS production (Figure 7e,f). Notably, the expression of antioxidant enzymes, glutathione peroxidase 1 (GPX1) and superoxide dismutase 2 (SOD2), was also suppressed by OcuTAPE (Figure 7g,h), suggesting an overall reduction in oxidative stress milieu. In contrast, Histoacryl did not alleviate oxidative stress, as gene expression levels for both pro-oxidant and antioxidant markers remained comparable to the LPS-injected group. This aligns with its observed pro-inflammatory effects and indicates a lack of therapeutic efficacy.

To further validate the ROS-scavenging activity of our treatment groups, we conducted immunofluorescence staining on retinal cryosections targeting SOD2 and 8-hydroxy-2′-deoxyguanosine (8-OHdG), two widely recognized markers of oxidative DNA damage.<sup>[82]</sup> Our results show that eyes treated with blank OcuTAPE, Dex-loaded OcuTAPE, or free Dex exhibited markedly reduced expression of both SOD2 and 8-OHdG compared to LPS-injected untreated mice and those treated with Histoacryl (Figure 7i). These findings provide direct evidence that OcuTAPE mitigated oxidative stress in inflamed retinal tissue, highlighting its localized antioxidant effect in vivo.

Importantly, no significant differences were observed among OcuTAPE, Dex-loaded OcuTAPE, and free Dex in oxidative stress markers, indicating that blank OcuTAPE possessed inherent ROS-scavenging activity. This intrinsic bioactivity helps explain its standalone anti-inflammatory effects and highlights its potential for steroid-sparing therapeutic strategies. Combined with its biocompatibility, mucoadhesion, and sustained release capability, OcuTAPE represents a promising noninvasive treatment platform for oxidative stress-related ocular diseases.

To evaluate the potential impact of oxidative stress on Ocu-TAPE's long-term stability and adhesive performance, the patch was exposed to 500  $\mu M\ H_2O_2$  for 2 h, a supraphysiological yet pathologically relevant concentration observed in inflamed ocular environments. [83] Although this duration does not replicate chronic exposure, it serves as an accelerated condition to simulate oxidative stress-induced degradation. Oxidation of TA's phenolic groups can reduce hydrogen bonding capacity; accordingly, a modest decrease in adhesive strength (\*p < 0.05) was observed (Figure S14b, Supporting Information), suggesting partial consumption of TA. Nonetheless, the patch retained strong adhesion, indicating that the adhesive network remained functionally stable under oxidative challenge. Notably, mild oxidation of TA may also generate quinones capable of forming

16163028, 0, Downloaded from https

onlinelibrary.wiley.com/doi/10.1002/adfm.202516281 by University Of California, Los Angeles, Wiley Online Library on [2208/2025]. See the Terms

and Conditions (https://onlinelibrary.wiley.com/terms

and-conditions) on Wiley Online Library for rules of use; OA articles are governed by the applicable Creative Commons

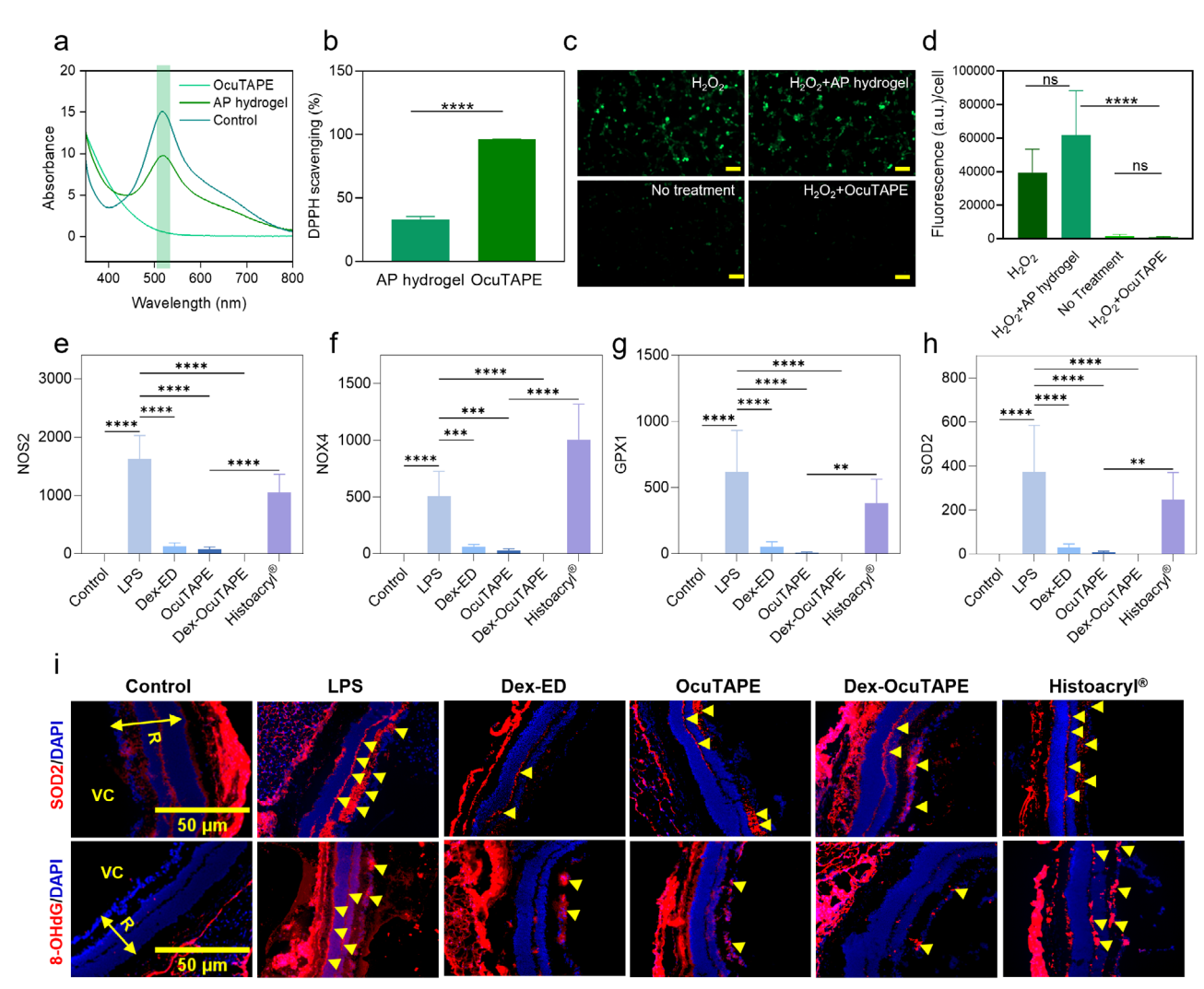


Figure 7. In vitro and in vivo reactive oxygen species (ROS)-scavenging effects of OcuTAPE. In vitro evaluations: a) absorbance change (n = 4) of DPPH• before and after the reaction at 517 nm. b) The % of DPPH• scavenging for the AP hydrogel and OcuTAPE. c) Representative ROS stained (green fluorescence) images of 3T3 cells (n = 6) with no treatment or treated with  $H_2O_2$  and  $H_2O_2$  in combination with the AP hydrogel or OcuTAPE to assess intracellular ROS activity (scale bars: 100 µm). d) Quantitative analysis of DCFH-DA fluorescence intensity in 3T3 cells with different treatments. in vivo evaluations: e−h) quantitative PCR analysis of retinal tissue 24 h post-treatment in vivo showing relative mRNA expression levels of oxidative stress-related enzymes: inducible NOS2, NOX4, GPX1, and SOD2. Treatment with blank OcuTAPE, Dex-loaded OcuTAPE, or Dex eye drops (Dex-ED) significantly reduced the expression of NOS2, NOX4, GPX1, and SOD2 compared to the LPS-treated and Histoacryl-treated group. i) Representative immunofluorescence images of retinal cryosections immunostained for SOD2 and 8-OHdG. Treatment with blank OcuTAPE, Dex-loaded OcuTAPE, or free Dex showed decreased SOD2 and 8-OHdG labelling compared to LPS-only control and Histoacryl-treated group (a few representative stained cells are marked with yellow arrows), confirming ROS scavenging of OcuTAPE at the tissue level. R: retina, VC: vitreous chamber/cavity. The bar graph represents the mean  $\pm$  SD of six mice/group. \*\*p < 0.001; \*\*\*\*\*p < 0.0001; ns = not significant (t-test or one-way ANOVA). n = 6.

covalent interactions with tissue. These results support the potential of OcuTAPE to maintain functional performance under inflammatory conditions, with TA contributing both therapeutic effects and adhesion robustness.

### 2.8. Demonstration of TA-Bridged PLGA-GelMA Nanocomposites for Drug Delivery

To demonstrate the versatility of our TA-bridging strategy, we developed a second NP-hydrogel system composed of PLGA NPs embedded within a GelMA matrix. This formulation also

employed TA to enable stable NP incorporation through dynamic hydrogen bonding and hydrophobic interactions. In contrast to the MC-OcuTAPE system optimized for ocular delivery, this platform combines biodegradable PLGA NPs with GelMA, an extracellular matrix-mimicking hydrogel widely used in tissue engineering. TA forms multiple hydrogen bonds with the amide and hydroxyl groups present on GelMA chains,<sup>[39]</sup> establishing a physically crosslinked network without the need for chemical modification. This non-covalent GelMA-TA interaction forms the structural basis of the hydrogel, while also providing abundant phenolic groups for secondary interactions with NPs. This model allowed us to evaluate the generalizability of

1616280.8, D. Dowloaded from https://advanced.onlinelbray.wiley.com/doi/10.1002/adfm.202316281 by University Of California, Los Angeles, Wiley Online Library on [22.08.2025], See the Terms and Conditions (https://onlinelibrary.wiley.com/terms-and-conditions) on Wiley Online Library for rules of use; OA articles are governed by the applicable Creative Commons

www.afm-journal.de

TA-mediated NP retention and sustained drug release in a structurally and functionally distinct setting, supporting its broader applicability. As a proof of concept, we encapsulated Cur, an extensively studied natural therapeutic compound with potent anticancer, anti-inflammatory, antioxidant, and antimicrobial properties, into PLGA NPs. Cur is widely used in drug delivery research as a clinically relevant yet formulation-challenging compound due to its poor aqueous solubility, low bioavailability, and rapid degradation. These features make it an ideal candidate for assessing a system's capacity to enhance drug stability and provide sustained release. Additionally, Cur's intrinsic fluorescence enables label-free tracking of NP localization and drug release, further reinforcing its value as a mechanistically relevant and experimentally tractable model.

To investigate the molecular interactions underlying NP incorporation into the hydrogel network, high-resolution XPS analysis was performed on PLGA NPs, GelMA-TA hydrogel, and the resulting GelMA-TA-PLGA nanocomposite (Figure 8a,b,c). The C 1s spectrum of the GelMA-TA hydrogel exhibited a characteristic  $\pi - \pi^*$  satellite peak (Figure 8bi), consistent with the presence of aromatic phenolic structures in TA. This satellite signal was notably diminished in the GelMA-TA-PLGA composite (Figure 8ci), indicating that the electronic environment of TA's aromatic rings was perturbed upon NP incorporation. Since PLGA lacks aromatic structures capable of engaging in  $\pi$ - $\pi$  stacking, the observed spectral shift is more likely the result of hydrogen bonding or hydrophobic interactions between TA and the PLGA NP surface, which can disrupt or shield the  $\pi$ -electron system of TA. Such a disappearance of the  $\pi$ - $\pi$ \* satellite has been previously interpreted as evidence of disrupted aromatic interactions in TA systems lacking sufficient aromatic moieties to support effective  $\pi - \pi$  stacking.<sup>[85]</sup> Further deconvolution of the C 1s spectra revealed distinct shifts in carbon bonding environments. In GelMA-TA, a higher proportion of C-O was observed relative to O-C=O, consistent with the abundance of hydroxyl functionalities from GelMA side chains and TA's phenolic groups (Figure 8bi). Upon incorporation of PLGA NPs, a significant increase in the O-C=O peak was observed (Figure 8ci), consistent with the contribution of ester carbonyl groups from the PLGA structure (Figure 8ai). Additionally, the C=O peak, attributed to amide carbonyls in GelMA and oxidized quinone forms in TA, decreased significantly in the GelMA-TA-PLGA nanocomposite (Figure 8ci). This reduction is consistent with PLGA's chemical composition, which lacks free carbonyl (C=O) groups and instead presents ester functionalities. Moreover, a pronounced increase in the C−C/C−H peak (≈284.8 eV) was observed in the composite, corresponding to the aliphatic chains of the PLGA backbone, further confirming successful NP integration.

O 1s spectra provided complementary evidence. PLGA NPs displayed nearly equal contributions from C—O and C=O oxygen species (Figure 8aii), consistent with the presence of both ester groups (—COO—) and additional C—O-containing functionalities within the PLGA (50:50) backbone. In contrast, the GelMA-TA hydrogel exhibited a dominant C—O signal (Figure 8bii), reflecting the high hydroxyl content of TA and GelMA. Following NP incorporation, the O 1s profile of the GelMA-TA-PLGA nanocomposite shifted toward an intermediate state between the two (Figure 8cii), with a more balanced distribution of C—O and C=O contributions. This redistribution of oxygen environments

likely results from the relatively high loading of ester-rich PLGA NPs within the hydrogel matrix and supports their stable integration into the network.

Following XPS characterization, we examined the physicochemical properties and functional performance of the GelMA-TA-PLGA nanocomposite system. As shown in Figure 8d, successful loading of Cur into PLGA NPs resulted in an increase in hydrodynamic diameter from 245.4 ± 3.9 nm (PDI: 0.13 ± 0.01) for unloaded PLGA NPs to 274.5  $\pm$  9.9 nm (PDI: 0.30  $\pm$ 0.07) for Cur-loaded PLGA NPs, reflecting effective encapsulation with a modest increase in particle heterogeneity. Zeta potential measurements (Figure 8e) revealed that both unloaded and drug-loaded NPs carried negative surface charges ( $-15.9 \pm$ 0.6 mV and  $-10.1 \pm 0.7 \text{ mV}$ , respectively), primarily due to the ionized carboxylic acid end groups in PLGA. The less negative surface potential after drug loading likely resulted from partial shielding of the negatively charged carboxylate end groups on the PLGA surface by the hydrophobic Cur molecules, which may adsorb or associate near the NP surface.

To assess NP incorporation into the hydrogel matrix, the GelMA-TA hydrogel was immersed in a solution of Cur-loaded PLGA NPs. As shown in Figure 8f, a substantial drop in solution absorbance was observed after 5 h, indicating efficient depletion of NPs from the surrounding medium due to their crosslinking into the hydrogel network. This was accompanied by a distinct visual transformation of the hydrogel from a lightly transparent state to an opaque orange color, consistent with the accumulation of Cur-loaded NPs within the matrix. Time-lapse imaging (Figure 8g) further supported this observation, showing the gradual clarification of the NP solution over time, indicative of sustained and progressive NP uptake into the GelMA-TA hydrogel.

Taking advantage of the intrinsic fluorescence of Cur, confocal fluorescence imaging was employed to directly visualize and confirm the spatial retention of NPs within the hydrogel matrix (Figure 8h). A strong Cur-PLGA NP signal was observed throughout the GelMA-TA hydrogel (Figure 8hi). The 3D reconstruction demonstrated that the NPs primarily localized within the porous regions of the 3D network with a relatively homogeneous distribution within the observable imaging depth (Figure 8hi-i-iii; Video S4, Supporting Information). Scanning electron microscopy (SEM) corroborated these findings, revealing dense incorporation of NPs within the cross-sectional structure of the GelMA-TA hydrogel following immersion in the NP solution (Figure 8i). In contrast, GelMA hydrogels lacking TA exhibited minimal NP retention, highlighting the essential role of TA in mediating NP-hydrogel interactions.

Finally, we evaluated the loading and release behavior of the nanocomposite system (Figure 8j,k). Cur demonstrated high encapsulation efficiency (>75%) into PLGA NPs and was further retained within the GelMA-TA hydrogel with high loading efficiency (>95%) (Figure 8j). Notably, most NPs were successfully entrapped within the hydrogel network, although a small fraction appeared to precipitate near the gel surface. The release profile showed sustained, controlled release of Cur over 42 days, with a cumulative release of  $\approx$ 42.7% (Figure 8k). The absence of burst release and prolonged kinetics was attributed to both the diffusion-limited release from PLGA and the TA-mediated physical bridging of NPs within the hydrogel matrix. These findings highlight the potential of TA as a versatile supramolecular binder

16163028, 0, Downloaded from https://advancec

onlinelibrary.wiley.com/doi/10.1002/adfm.202516281 by University Of California, Los Angeles, Wiley Online Library on [22/08/2025]. See the Terms

on Wiley Online Library for rules of use; OA articles are governed by the applicable Creative Commons

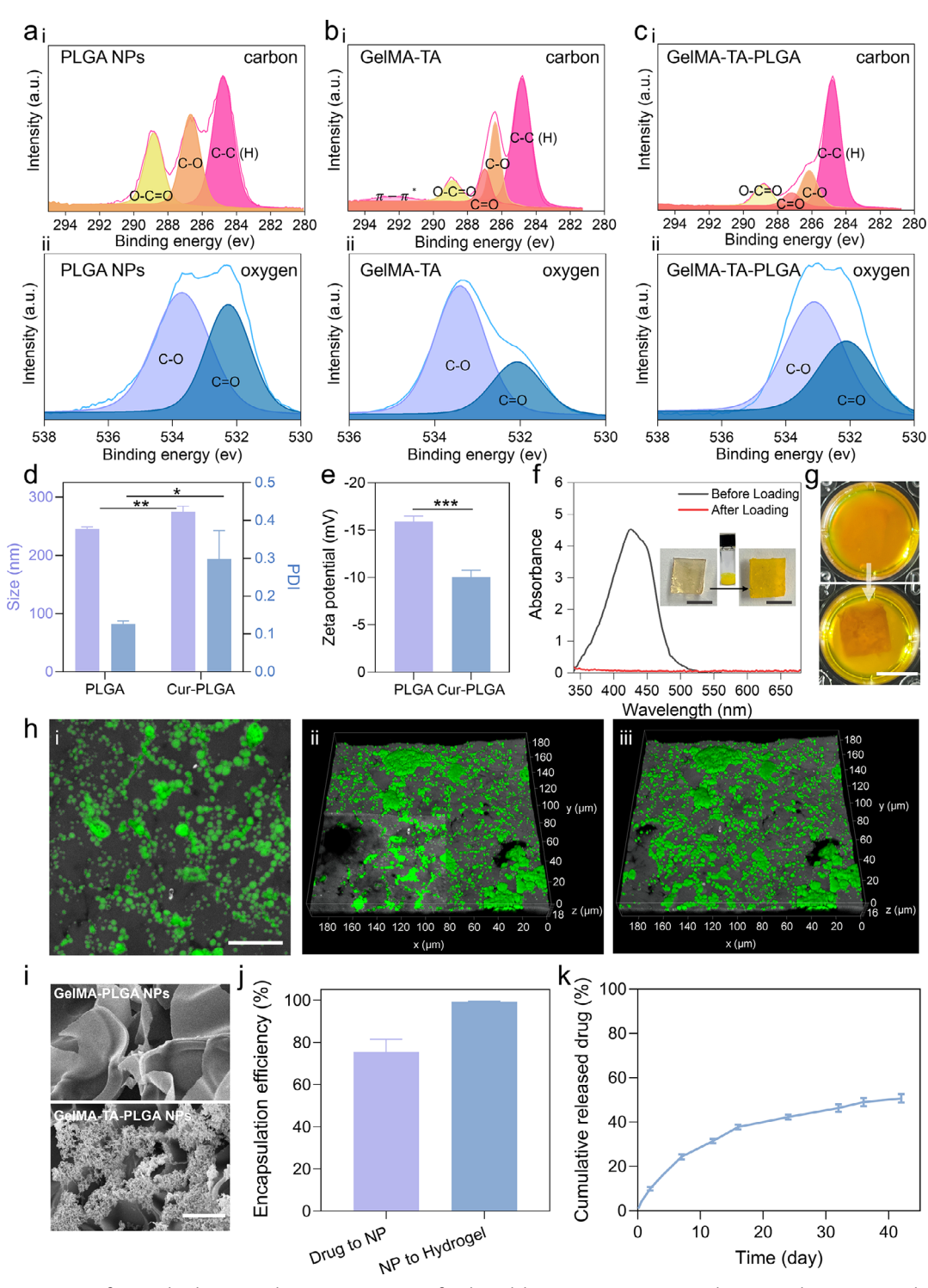


Figure 8. Demonstration of TA-Bridged PLGA-GelMA nanocomposite for drug delivery. a-c) XPS spectra showing carbon (ai-ci) and oxygen signals (aii-cii) for (ai-ii) PLGA NPs, (bi-ii) GelMA-TA hydrogel, and (ci-ii) GelMA-TA-PLGA nanocomposite. d) Size, PDI, and e) zeta potential of PLGA NPs and Cur-loaded PLGA NPs. f) Absorbance spectra of PLGA NPs before and after crosslinking with GelMA-TA hydrogel, alongside digital images of GelMA-TA hydrogel before and after incorporation of Cur-loaded PLGA NPs. Scale bar: 5 mm. g) Digital images of Cur-loaded PLGA NPs before and after crosslinking with GelMA-TA hydrogel, confirming successful NP integration. Scale bar: 5 mm. h) Confocal microscopy images of GelMA-TA hydrogel after crosslinking with Cur-loaded PLGA NPs: i) 2D confocal image (scale bar: 25 µm), ii) 3D cross-sectional view, and iii) 3D confocal image showing the surface and internal distribution of NPs within the imaging depth. (i) SEM images of GelMA hydrogel and GelMA-TA hydrogel after immersion in PLGA NP solution, showing enhanced NP retention in the TA-containing hydrogel. Scale bar: 10 µm. j) Encapsulation efficiency of Cur into PLGA NPs and subsequent loading efficiency of Cur-loaded PLGA NPs into GelMA-TA hydrogel. k) Cumulative release profile (%) of Cur from the GelMA-TA-PLGA nanocomposite. Data are presented as mean  $\pm$  SD. \*p < 0.05; \*\*p < 0.01; \*\*\*p < 0.001; ns = not significant (t-test). n  $\geq$  3.



www.afm-journal.de

1616280.8, D. Dowloaded from https://advanced.onlinelbray.wiley.com/doi/10.1002/adfm.202316281 by University Of California, Los Angeles, Wiley Online Library on [22.08.2025], See the Terms and Conditions (https://onlinelibrary.wiley.com/terms-and-conditions) on Wiley Online Library for rules of use; OA articles are governed by the applicable Creative Commons

capable of mediating stable and homogeneous NP incorporation throughout hydrogel networks, enabling the design of multifunctional biomaterials that combine structural support, bioactivity, and controlled therapeutic delivery, an approach broadly applicable to regenerative medicine, tissue repair, and localized treatment of diseases.

#### 3. Discussion

OcuTAPE presents an effective solution to the limitations of traditional ocular adhesives, addressing key challenges such as long-term adhesion, ease of application, and mechanical compatibility with ocular tissues. The dual adhesive moieties of the patch, NHS and mussel-inspired functional groups of TA, were adopted for achieving enhanced adherence to wet ocular tissue. NHS is known to possess high reactivity and form covalent interactions with tissue surfaces. [38,39,48,86] The presence of catechols/pyrogallols in TA, the moieties mimicking adhesive foot proteins of marine mussels to provide wet adhesion underwater,[39] contributes to enhanced mucoadhesion. Its ability to conform seamlessly to the ocular surface, withstand the mechanical stresses of blinking, and remain securely in place without causing discomfort makes OcuTAPE an ideal adhesive for sealing ocular injuries and serving as a matrix for local delivery of therapeutics. Notably, OcuTAPE not only functions as a physical sealant and drug delivery platform but also possesses intrinsic therapeutic properties, owing to the antioxidant and antiinflammatory nature of TA. This represents a critical distinction, as most existing ocular adhesive materials primarily serve as passive sealants and do not provide inherent therapeutic benefits. To the best of our knowledge, few, if any, available ocular adhesives exhibit such bioactive functionalities.

In conventional systems, physically embedding nanomaterials into hydrogels often results in uncontrolled release, early-stage drug loss, and potential tissue toxicity. [2,87] OcuTAPE's use of TA as a crosslinker for MCs within the hydrogel matrix enabled precise control over drug release, making it ideal for sustained therapeutic delivery. While OcuTAPE has demonstrated significant clinical translational potential, further studies will be needed to evaluate its long-term efficacy and explore its potential applications in treating a wider range of ocular conditions, including glaucoma, uveitis, and others. Additionally, the patch was originally optimized for porcine eyes, which closely resemble human ocular anatomy in size and curvature. While it was well tolerated in rabbits, occasional mild responses were observed in mice, likely due to their smaller eye size and greater curvature mismatch, which can increase local mechanical stress. No signs of inflammation or tissue damage were observed in larger-eye models, supporting the biocompatibility of the patch in clinically relevant settings. This highlights the importance of tailoring patch geometry and hydration status to the specific anatomical context, particularly when translating to small-animal models.

While the present study focuses on ocular drug delivery, the hydrogel-NP platform described here may be adaptable to other anatomical sites that demand conformability, strong wet adhesion, and sustained local drug delivery. With appropriate adjustments to hydrogel composition, such as modulating stiffness, adhesiveness, and release kinetics, this system could potentially be applied to diverse soft internal tissues, including surgical wounds

and mucosal linings such as those in the gastrointestinal and respiratory tracts, as well as vaginal and cervical tissues. These environments, like the ocular surface, present unique mechanical and biological challenges that may benefit from a similarly tunable and synthesis-free material strategy. Although additional studies would be needed to validate such applications, we demonstrated the adaptability of the TA-bridging approach by applying it to a distinct nanocarrier-hydrogel combination: Cur-loaded PLGA NPs crosslinked within a GelMA-TA matrix. Unlike Ocu-TAPE, which leverages PEG-based MCs and a dual-polymer network tailored for ocular applications, this secondary system utilizes a biodegradable NP and a naturally derived, bioactive hydrogel with broad relevance in regenerative medicine. Despite differences in material chemistry and intended application, the PLGA-GelMA composite similarly benefited from TA-mediated integration, exhibiting stable NP retention and sustained drug release. These results not only validate the mechanistic generalizability of TA-bridging beyond a single formulation but also illustrate its adaptability to various therapeutic contexts.

The bridging efficiency of TA is highly context-dependent and influenced by multiple parameters, including the chemistry of TA-NP and TA-hydrogel interactions, crosslinking time, hydrogel crosslinking density and pore size, as well as NP size. For example, a more densely crosslinked hydrogel may restrict NP penetration due to reduced pore size, while variations in NP surface chemistry (e.g., PLGA NPs vs PEG-based MCs) can modulate the strength and specificity of TA-mediated interactions. This work serves as a proof-of-concept demonstration of TA-bridged nanocomposite formation. Future studies will systematically explore these variables to optimize NP incorporation and fully elucidate the underlying structure-function relationships.

#### 4. Conclusion

In this study, we present OcuTAPE as a multifunctional ocular patch that combines wet tissue adhesion, tissue-mimicking mechanics, therapeutic activity, and sustained drug release through TA-mediated NP bridging. By enabling robust NP incorporation without covalent modification or complex synthesis, this approach may offer a promising direction for developing diverse nanocomposite bioadhesives, ranging from anti-inflammatory ocular patches to tissue-regenerative scaffolds, using clinically compatible building blocks.

#### 5. Experimental Section/Methods

Materials: Polyethylene glycol (PEG, 20 kDa), sodium salt of alginic acid from brown algae (Alg, 30–100 kDa), tannic acid (TA), hydroquinone, acryloyl chloride, triethylamine and lithium phenyl-2,4,6-trimethylbenzoylphosphinate photoinitiator (LAP), lipopolysaccharides (LPS), curcumin (Cur), polyvinyl alcohol (PVA, 31–50 kDa) were acquired from Sigma-Aldrich. 1-(3-Dimethylaminopropyl)-3-ethylcarbodiimide hydrochloride (EDC), N-Hydroxysuccinimide (NHS), β-cyclodextrin (β-CD) were purchased from TCI Chemicals. Calcium chloride was purchased from Acros Organic. Dexamethasone (Dex) and latanoprost (LP) were obtained from TCI chemicals. Dex eye drop (0.1% ophthalmic) was from Bausch + Lomb. Poly (lactic-co-glycolic acid), 50:50, was purchased from Polyscience. Dulbecco's modified Eagle medium (DMEM) was purchased from Cellgro (Manassas, VA). Fetal bovine

16163028, 0, Downloaded from https://advanced.onlinelibrary.wiley.com/doi/10.1002/adfm.202516281 by University Of California, Los Angeles, Wiley Online Library on [22/08/2025]. See the Terms and Conditions (https://onlinelibrary.wiley.com/erms-

and-conditions) on Wiley Online Library for rules of use; OA articles are governed by the applicable Creative Commons

serum (FBS) and DPBS were obtained from HyClone (Logan, UT). Penicillin/streptomycin (Pen-Strep), Live/Dead viability kit were purchased from Invitrogen, Thermo Fisher Scientific. H2O2 was purchased from Fisher Chemicals. 4,4-Azobis (4-cyanopentanoic acid) (ABCPA), poly (ethylene glycol) methyl ether (Mw 5000 g mol<sup>-1</sup>) (mPEG), N,N'-Dicyclohexylcarbodiimide (DCC), 4-dimethylaminopyridine (DMAP), ptoluenesulfonic acid, L-lactide, N-(2-hydroxypropyl) methacrylamide (HP-MAm), Tin(II) 2-ethylhexanoate (SnOct2), 4-methoxyphenol, Oil Red O and diacetyldichlorofluorescein (DCFH-DA) were purchased from Sigma-Aldrich. All solvents: tetrahydrofuran (THF), dichloromethane (DCM), dimethylformamide (DMF), acetonitrile (ACN), hexane, toluene, and acetone were purchased from Sigma-Aldrich or Fisher Chemical. Nuclear magnetic resonance (NMR) solvents: chloroform-d (CDCl<sub>3</sub>), deuterated dimethyl sulfoxide (DMSO-d6) and deuterium oxide (D2O) were purchased from Cambridge Isotope Laboratories, Inc. Gelatin from porcine skin (Gel strength 300, type A), Rhodamine B, methacrylic anhydride, Eosin Y disodium salt, triethanolamine (TEA) and N-vinylcaprolactam (VC), Triton X-100 were all purchased from Sigma-Aldrich. The qPCR gene-specific primers for the pro-inflammatory cytokines (IL-1 $\beta$ , IL-6) and chemokines (CCL-2, CXCL-1, CXCL-2, CXCL-5, CXCL-10) were synthesized from Integrated DNA Technologies (Coralville, IA). The gene primer sequence was listed in Table S2 (Supporting Information).

Synthesis of Polyethylene Glycol (PEG) Diacrylate (DA): PEGDA (20 kDa) was selected based on prior findings showing optimal adhesion strength when combined with TA, due to favorable hydrogen bonding and chain entanglement.<sup>[38]</sup> Initially, PEGDA was synthesized in toluene through the chemical conjugation of PEG and acryloyl chloride, following a previously described method.<sup>[88]</sup> First, 30 g of PEG (20 kDa) was dissolved in toluene and combined with 2.5 mL of triethylamine. Subsequently, 1 mL of acryloyl chloride and 10 mL of dried toluene were introduced to the reaction mixture and allowed to react for 2 h. The resulting mixture underwent filtration through a silica bed and was filtered into a flask containing 200 µL of a 30-50 ppm hydroquinone solution in acetone. A molar ratio of PEG: acryloyl chloride: triethylamine = 1:8.1:11.9 was used during the PEGDA synthesis. The synthesized PEGDA was then precipitated in hexane and stored at -80 °C for future use. The acrylation was confirmed through <sup>1</sup>H NMR, with an efficiency rate calculated at 93%.

Synthesis of Alginate-N-Hydroxysuccinimide (Alg-NHS): Alg-NHS was synthesized from alginic acid sodium salt by esterifying its native carboxyl (—COOH) functional groups following a previously described method. [33] Initially, 1 g of Alg was dissolved in 100 mL of Milli-Q water. Afterward, molar ratios of EDC and NHS were added dropwise into the solution, stirred for 2-3 h on a 45 °C hotplate (Molar ratio: -COOH (in Alg): EDC: NHS = 1:4:20). The resulting product was precipitated by the addition of chilled 95% ethanol. Following precipitation, the product underwent thorough washing with pure ethanol and was subsequently lyophilized through freezing for 24 h and then freeze-drying for another 24 h. <sup>1</sup>H NMR analysis was utilized to validate the chemical functionalization of Alg using a 400 MHz Bruker AV400 spectrometer. The samples were prepared by dissolving  $\approx 10$  mg of the dried polymers in 0.7 mL of D<sub>2</sub>O.

OcuTAPE Synthesis and Characterization: OcuTAPE hydrogel was synthesized using a previously published protocol with slight modifications. A  $0.5~{\rm mg~mL^{-1}}$  solution of LAP in MilliQ was prepared in the absence of light. Then, Alg-NHS (4%, w/v) was dissolved in this solution on a hot plate at 250 rpm at room temperature for 1 h under dark conditions. PEGDA (22%, w/v) was then dissolved under the same conditions to form the prepolymer solution. The prepolymer solution was cast into PDMS molds and crosslinked under UV-vis light (405 nm) for 4 min, forming the Alg-NHS and PEGDA (AP) hydrogel network. The hydrogels were then removed from the molds and placed in a TA and calcium solution to chemically crosslink for 24 h in dark conditions. The crosslinking solution, containing 40% (w/v) TA and 3% (w/v) Ca<sup>2+</sup> in MilliQ water, was prepared. After crosslinking, the OcuTAPE hydrogels were rinsed thoroughly with water to remove uncrosslinked solution, desiccated to a semi-dry state, which preserves their flexibility and readiness for application, vacuum sealed, and stored at 4 °C until further experimentation was needed. An XPS (AXIS Ultra DLD instrument) was employed to analyze the chemical composition of the OcuTAPE hydrogel. A monochromatic Al K $\alpha$  X-ray at 15 kV and 10 mA served as the excitation source, and the neutral C 1s peak (C—C (H) set at 284.6 eV) was used as a reference for charge correction. Rheological investigations were performed using a Modular Compact Rheometer MCR302 to characterize the intermolecular interactions. The results were obtained by linking the measuring system PP08 with a diameter of 8 mm to the rheometer. Each measurement was carried out by loading a fresh sample in the 1 mm gap between the parallel plates and removal of excessive sample. A strain amplitude sweep (0.01%-10000%) was performed at a constant frequency of 10 rad/s. Subsequently, a frequency sweep (1-100 rad/s) was carried out at a shear strain of  $\gamma = 1\%$  to record the storage modulus (G') and loss modulus (G"). All measurements were performed at room temperature (25 °C).

In Vitro Mechanical Characterizations: OcuTAPE samples were equilibrated in DPBS at 37 °C for 1 h to assess the mechanical characteristics of the swollen hydrogels. The tensile properties of the OcuTAPE hydrogels were evaluated through tensile tests conducted on thin rectangular samples (10 mm in length, 3 mm in width, 0.9 mm in thickness, with precise dimensions measured using a digital caliper) using a mechanical testing machine (Instron 5943). In all tests (n  $\geq$  4), the tensile speed was set at 50 mm min<sup>-1</sup>.

Fresh porcine conjunctival tissues underwent testing using the same method immediately after harvesting. The ultimate strength was defined as the stress at the failure point, with the strain recorded from the same location. For all samples, Young's modulus was determined from the slope of 1/6-1/5 of the strain in the stress-strain curve, while toughness was calculated as the area under the stress-strain curve. In the case of fresh porcine conjunctiva tissues, Young's modulus was calculated from the initial linear region of the stress-strain curve.

Cylindrical gel samples were used for compression tests. A cyclic compression test was performed up to 50% strain at a constant compression speed of 50%  $min^{-1}$  over 60 cycles (n = 3). Dissipated energy was calculated by measuring the area of the hysteresis loop. The cylindrically shaped OcuTAPE samples (with precise dimensions measured using a digital caliper) were immersed in DPBS during the test. All the data from Instron was recorded using Bluehill 4.06 software.

In vitro Swelling Study: 100  $\mu$ L OcuTAPE (n = 5) and AP (n = 5) hydrogel liquid precursor cast in cylindrical PDMS molds were placed in a 24 well plate containing DPBS at 37 °C to observe the swelling profile of the hydrogels over various time points (0, 0.25, 1, 2, 3.5, 19, 24, 48, 72, 96, 120 h). The initial weights of the hydrogels were taken prior to submergence into DPBS, and swelling weights were confirmed by first removing excess liquid from the hydrogel surface and then weighing.

In vitro Adhesive Characterizations: In the adhesive lap shear test (ASTM F2255) and wound closure test (ASTM F2458), fresh porcine conjunctival tissue surfaces were used. Following patch adherence to the tissues, firm pressure was applied for 1 min before placing it in a 37 °C incubation oven for 15 min to reach equilibrium and simulate physiologically relevant temperatures. Subsequently, a mechanical testing machine (Instron 5943) was employed to test the adhered samples for the lap shear test (18 mm in length x 7.5 mm in width), and wound closure test (3.1 mm in width x 0.8 mm in thickness) with precise dimensions measured using a digital caliper. All tests (n  $\geq$  4) were carried out with a constant tensile speed of 50 mm min<sup>-1</sup>, and shear strength was determined by dividing the maximum force by the adhesion area. The adhesive strength determined through the wound closure test was calculated by dividing the maximum force by the cross-sectional area. During the lap shear and wound closure tests, conjunctival tissues were affixed to glass slides using cyanoacrylate glue to immobilize the tissue and enable consistent adhesion testing with the hydrogels. The lap shear and wound closure tests were also performed on Histoacryl, composed of n-butyl-2-cyanoacrylate, using the same procedure as previously described. To investigate the impact of pressing and incubation time on the adhesive strength of OcuTAPE, the hydrogel was adhered to conjunctival tissue and tested under different conditions. Incubation times of 0, 15, and 120 min were applied with a fixed pressing time of 1 min, while pressing times of 0, 1, and 3 min were tested with no incubation time using a lap shear test. Additionally, the repositionability of OcuTAPE was evaluated by performing 11 consecutive lap shear tests,

1616280.8, D. Dowloaded from https://advanced.oninelbray.wiley.com/doi/10.1002/adfm.202316281 by University Of California, Los Angeles, Wiley Online Library on [22:08:2025], See the Terms and Conditions (https://onlinelibrary.wiley.com/terms-and-conditions) on Wiley Online Library for rules of use; OA articles are governed by the applicable Cerative Commons.

measuring any changes in its shear strength when adhered to conjunctival tissue.

In vitro Antioxidant DPPH ◆ Assay: The antioxidant effectiveness of the prepared hydrogels was measured using a method designed to neutralize the stable free radical 1,1-diphenyl-2-picrylhydrazyl (DPPH ◆). [89] DPPH ◆ was dissolved in ethanol, creating a 0.2 mmol L<sup>-1</sup> solution. Cylindrical samples of OcuTAPE and AP hydrogel, each 2 mm in diameter and 0.5 mm in thickness, were added to 1 mL of the DPPH ◆/ ethanol solution. The mixture was then placed on a vibrating shaker at 70 rpm and kept in the dark for 5 min. Absorbance was recorded at 517 nm using a UV−vis spectrophotometer (NanoDrop One/OneC), and the DPPH radical scavenging rate was determined using Equation (1):

DPPH • scavenging % = 
$$\frac{(A_0 - A_1)}{A_0} \times 100\%$$
 (1)

where  $A_0$  was the absorption of the DPPH $\bullet$  solution, and  $A_1$  was the absorption of the DPPH $\bullet$  solution after reacting with the hydrogel samples.

In Vitro Cytocompatibility Assay: The cytocompatibility of the engineered hydrogels was assessed by examining the in vitro viability and metabolic activity of NIH 3T3 fibroblasts utilizing Corning Costar Transwell cell culture inserts. Commercial Live/Dead kits (Invitrogen) and Actin/(4',6-diamidino-2-phenylindole) DAPI staining (Invitrogen) were employed to evaluate cell viability and proliferation, respectively. Metabolic activity was determined using a PrestoBlue (Life Sciences) assay. NIH 3T3 cells were seeded on the bottom of a 24-well Transwell permeable support (Costar, 8  $\mu$ m PET membrane) at a cell density of 1  $\times$  10<sup>4</sup> cells/well. OcuTAPE (~2 mm diameter, 0.5 mm thickness, cylindrical-shaped hydrogel) hydrogels prepared following the previously described protocol were placed into the Transwell inserts. Additionally, 1.5 mL of growth medium (Dulbecco's Modified Eagle's Medium) was added to each well of the Transwell permeable supports. The well plates were maintained at 37 °C in a humid 5% CO<sub>2</sub> environment for 5 days, with the culture medium replaced every 48 h.

The viability of 3T3 cells grown on the bottom of well plates was examined using a Live/Dead viability kit following the manufacturer's instructions (n = 4). Cells were briefly stained with 0.5  $\mu$ L mL<sup>-1</sup> of calcein AM and 2 µL mL<sup>-1</sup> of ethidium homodimer-1 (EthD-1) in DPBS for 20 min at 37 °C. Fluorescent imaging was conducted on the 1st, 3rd, 5th, and 7th day post-seeding using an AxioObserver Z7 inverted microscope. Viable and dead cells were distinguished by their green and red colors, respectively, and quantified using ImageI software. Cell viability was determined as the number of live cells divided by the total number of cells. The metabolic activity of the cells was evaluated on the 1st, 3rd, and 7th day post-seeding using a PrestoBlue assay (Life Technologies) (n = 6). 3T3 cells were incubated in 400 µL of 10% (v/v) PrestoBlue reagent in growth medium for 45 min at 37  $^{\circ}\text{C}\text{,}$  and fluorescence was measured using a Synergy HT fluorescence plate reader (BioTek). F-actin and cell nuclei were used to visualize the spreading of 3T3 cells at the bottom of the 24-well Transwell permeable supports (n = 4). Cells at days 1, 3, 5, and 7 post-seeding were fixed in 4% (v/v) paraformaldehyde (Sigma) for 15 min, permeabilized in 0.1% (w/v) Triton X-100 (Sigma) for 5 min, and blocked in 1% (w/v) bovine serum albumin (BSA, Sigma) for 30 min. Subsequently, samples were incubated with Alexa Fluor 488 phalloidin for 45 min. After repeated washes with DPBS, samples were counterstained with 1  $\mu L\,mL^{-1}$  of DAPI in DPBS for 2 min, and fluorescent imaging was performed using an inverted fluorescence microscope (Zeiss Axio Observer Z7).

Ex Vivo Adhesive Characterizations: A freshly isolated porcine eyeball was linked to a water pressure system and a Pascal sensor, with incisions introduced to induce leakages. On the conjunctiva of the eyeball, a 1.0 mm diameter incision was made using an ophthalmic knife (AccuSharp) to induce a leakage. Then, the OcuTAPE was applied with steady pressure for 1 min and left to adhere further for 15 min (n = 6). Subsequently, the water system was activated to introduce a pressure build-up at the site of the patched incisions in the eyeballs. The connected electronic pressure sensor measured the maximum pressure reached before either adhesive or tissue failure occurred. Histoacryl was used as a control and applied to seal conjunctival leakages according to the manufacturer's instructions.

Ex Vivo Automatic Blinker Study: OcuTAPE patches, GelMA, and commercial cyanoacrylate (Histoacryl) were adhered to rabbit eyeballs using various methods, and a mechanical lever (MG90S Micro Metal Gear Servo) was used to simulate blinking forces (n = 3). For application of OcuTAPE, rectangular prefabricated OcuTAPE patches (40 mm<sup>2</sup> in area, 0.9 mm thickness) prepared in the aforementioned sections were placed and pressed gently onto porcine conjunctiva for 1 min. Collagen sheets were placed on the other side of the OcuTAPE to prevent adhesion to the automatic blinker and tested after 15 min. For application of GelMA, 200 mg of GelMA was dissolved in 800  $\mu$ L TEA/VC solution, then mixed with 200 μL of Eosin Y and 2 μL of 5 mg mL<sup>-1</sup> Rhodamine B. Then, 50 μL of modified GelMA was photocured in situ for 4 min using a dental curing light and tested subsequently. For application of commercial cyanoacrylate, cyanoacrylate glue was applied according to the manufacturer's instructions and tested subsequently. During all tests, 50 µL of DPBS was applied every 5 min to the adhesion site until adhesive or cohesive failure

In Vitro Intracellular ROS Scavenging Activity: NIH 3T3 cells were seeded in 48-well plates at a density of  $3\times10^4$  cells per well and cultured for 24 h. To activate the cells,  $H_2O_2$  solutions (70  $\mu mol\ L^{-1}$ ) were added to the culture medium and incubated for 25 min. Subsequently, OcuTAPE or AP hydrogel (30  $\mu L$  of AP precursor solution) was introduced to the wells and incubated for an additional 30 min. Following this, the culture medium was replaced with fresh medium containing DCFH-DA solutions (100  $\mu mol\ L^{-1}$ ) and incubated for another 30 min. Green fluorescence signals in the cells were observed using a fluorescence microscope (Olympus, IX71), and the fluorescence intensity was quantified using ImageJ software.

MCs, Drug-loaded MCs, Drug-loaded OcuTAPE Synthesis and Characterizations—Synthesis of MCs: Synthesis of MCs was performed based on ourpreviously published protocol<sup>[25]</sup> which involved the synthesis of macroinitiator mPEG<sub>2</sub>-ABCPA, synthesis of monomer HPMAm-Lac<sub>n</sub>, synthesis of copolymer mPEG-b-p(HPMAm-Lac<sub>n</sub>), and preparation of unloaded and drug-loaded MCs.

Synthesis of macroinitiator mPEG $_2$ -ABCPA: Macroinitiators mPEG $_2$ -ABCPA were synthesized by esterifying mPEG with ABCPA using DCC as a coupling agent and DPTS as a catalyst, following the method of Bagheri et al.  $^{[90]}$  ABCPA (0.280 g), PEG (10 g), and DPTS (36.7 mg DMAP and 57.3 mg p-toluenesulfonic acid each in 1 mL THF) were dissolved in dry DCM on ice. After three vacuum-nitrogen cycles, DCC (0.619 g) in DCM was added dropwise under nitrogen, and the reaction proceeded at room temperature for 16 h. The mixture was filtered to remove 1,3-dicyclohexyl urea, dried under vacuum, redissolved in water, stirred for 2 h, dialyzed for 72 h at 4 °C, freeze-dried, and characterized by gel permeation chromatography (GPC) and  $^1$ H NMR.

Synthesis of monomer HPMAm-Lac $_n$ : HPMAm-Lac $_n$  monomer was synthesized following a previously reported method. [91] In summary, Llactide (5.0 g), HPMA (2.48 g), Sn (Oct) $_2$  (35.14 mg), and sodium sulfate (5 mg) were added to a round-bottom flask. The flask was subjected to a vacuum/ $N_2$  gas cycle at least three times to remove air. Subsequently, the flask was heated to 110 °C while stirring until complete dissolution of solids was achieved. The mixture was allowed to react at 110 °C for 18 h. After the reaction, the mixture was cooled to 25 °C and dissolved in THF. This solution was then precipitated into cyclohexane to remove any unreacted reagents. Finally, the precipitate was dried under vacuum overnight.

Synthesis of copolymer mPEG-b-p(HPMAm-Lac<sub>n</sub>): The mPEG-b-p(HPMAm-Lac<sub>n</sub>) copolymer was synthesized by radical polymerization using mPEG<sub>2</sub>-ABCPA as the macroinitiator and HPMAm-Lac<sub>n</sub> as the monomer at a feed ratio of 150:1.[92] Both components were dissolved in dry ACN at a concentration of 300 mg mL $^{-1}$ . The solution was degassed using freeze-pump-thaw cycles, heated to 70 °C, and stirred for 24 h. After cooling, the reaction mixture was diluted with ACN ( $\approx$ 2 mL) and precipitated into cold diethyl ether ( $\approx$ 45 mL). The precipitate was centrifuged at 3000 rpm for 15 min to form a white pellet, which was washed with diethyl ether and centrifuged three times. The product was dissolved in water, dialyzed (MWCO 12–14 kDa), and recovered by freeze-drying. The final product was characterized using GPC and  $^1$ H NMR.

ADVANCED
FUNCTIONAL
MATERIALS

16163028, 0, Downloaded from https://advanced.onlinelibrary.wiley.com/doi/10.1002/adfm.202516281 by University Of California, Los Angeles, Wiley Online Library on [22/08/2025]. See the Terms and Conditions (https://onlinelibrary.wiley.com/terms

and-conditions) on Wiley Online Library for rules of use; OA articles are governed by the applicable Creative Commons

Preparation of unloaded and drug-loaded MCs: In brief, 10 mg of the copolymer mPEG-b-p(HPMAm-Lac\_n) was dissolved in 1 mL of acetone. 1 mg of drug was added to the copolymer solution and vortexed until fully mixed. The polymer/drug mixture was then quickly added to 1 mL of ammonium acetate buffer (120 mM, pH = 5) with stirring. The solution was stirred at room temperature for 30 min, heated to 45 °C, and then slowly cooled and stirred overnight to slowly evaporate acetone. The next day, the solution was centrifuged at 2500 rpm at 22 °C for 5 min to remove unencapsulated drugs. Dex or LP were the drugs of interest, with 30 mg mL $^{-1}$  stock solutions prepared in DMSO. Unloaded MCs were prepared following the same procedure without adding drugs.

Dynamic Light Scattering (DLS) of MCs: Freshly prepared micellar dispersions were diluted with MilliQ water to reach a final concentration of 100  $\mu g\ mL^{-1}$ . The sizes of these dispersions were measured using a Malvern Zetasizer Nano dynamic light scattering device. The standard operating procedure involved conducting 10 runs, each lasting 10 s, with three measurements taken in succession without any delay, all at 25 °C with a 20 s equilibration time. The data presented represents the average of three replicate measurements. Zeta potential of the MCs was determined using a Malvern Zetasizer Nano-Z (Malvern Instruments, Malvern, UK) with zeta potential folded capillary cells (Malvern Panalytical) and DTS (Nano) software (version 4.20) at 25 °C. Zeta potential measurements were performed in MilliQ water at a final polymer concentration of  $100\,\mu g\ mL^{-1}$ .

Transmission Electron Microscopy (TEM) of MCs: The TEM images of MCs were taken using a T12 Quick room temperature TEM with a 120 kV electron-beam energy. The MC samples were dropped and dried on carbon-coated copper grids.

Loading Efficiency Characterization from Drug to MCs: The amount of the loaded Dex or LP within the polymeric MCs was determined using an HPLC. A standard curve was obtained using Dex or LP dissolved in ACN at concentrations ranging from 0.01 to 0.1 mg mL $^{-1}$ . The concentration of Dex or LP solutions was measured using HPLC with an ACN/water without acid gradient solvent system at 242 nm or 210 nm, respectively. Shimadzu Nexcol C18 1.8  $\mu$ m 50  $\times$  2.1 mm was used at 0.2 mL min $^{-1}$  flow rate, with a 70%–90% ACN gradient for 10 min. The set injection volume into the HPLC was 10  $\mu$ L per Dex sample and 50  $\mu$ L per LP sample. The freshly prepared drug-loaded MCs were centrifuged at 2500 rpm at 22 °C for 5 min to separate the unencapsulated Dex or LP pellet. Following the centrifugation process, the supernatant was carefully pipetted out. The Dex or LP pellet was dissolved in 10 mL of ACN. The loading efficiency (%) was calculated using Equation (2):

Load efficiency% = 
$$\left(1 - \frac{\text{unencapsulated drug}}{\text{total drug added}}\right) \times 100\%$$
 (2)

Preparation of MC-Loaded OcuTAPE and Loading Efficiency: After synthesizing the drug-loaded MCs, they were subsequently concentrated using a 30K MWCO protein concentrator (Thermo Scientific) by 10 times to make a highly concentrated MC solution. Afterward, OcuTAPE at different sizes were immersed in the concentrated MC solution for 90 min at room temperature for MC crosslinking. OcuTAPE was then gently rinsed with MilliQ water to remove excessive MC solution attached to its surface. To calculate the loading efficiency, the drug MC solution before and after crosslinking was diluted 100 times in ACN, and HPLC was used to quantify the drug concentration of MCs before and after crosslinking.

In Vitro Drug Releasing Study: In vitro release profiles of Dex from Ocu-TAPE were measured using artificial tears as the releasing medium. Ocu-TAPE samples of different sizes (7 mm² and 20 mm²) were immersed in 50 mL of artificial tears and incubated with shaking at 75 rpm at 37 °C. Samples (1 mL) of the receiving medium were drawn periodically, and fresh releasing medium were added back to keep the volume constant. The concentration of Dex in the different samples (n = 3) was measured by HPLC, as indicated above. The composition of artificial tear fluid used was sodium chloride 0.670 g, sodium bicarbonate 0.200 g, calcium chloride-2H<sub>2</sub>O 0.008 g, purified water q.s. 100.0 g, [93] pH 7.4. To evaluate MC stability under physiologically relevant ocular conditions, drug release studies were conducted using artificial tears adjusted to pH 6.5 (inflamed

ocular environment) and pH 7.4 (normal tears). Dex-loaded MCs were concentrated using a 30K MWCO protein concentrator (Thermo Scientific) to achieve a final Dex concentration of 1 mg mL $^{-1}$ . A total of 200  $\mu L$  of the MC solution was placed inside a Slide-A-Lyzer MINI Dialysis Device (10 kDa MWCO) and immersed in the corresponding buffer. Samples were incubated at 37 °C under gentle shaking. At predetermined time points, 1 mL of the release medium was collected and replaced with fresh buffer to maintain sink conditions. The amount of Dex released was quantified by HPLC, using a standard calibration curve prepared in ACN.

In Vitro Anti-Inflammatory Study: BMDM were seeded on the bottom of a 12-well Transwell plate (Corning Transwell 0.4  $\mu m$  PET membrane) at a cell density of 0.5  $\times$   $10^6$  cells/well. Inflammation was induced by challenging the cells with 100 ng  $mL^{-1}$  of LPS. Dex-loaded OcuTAPE (circular  $\approx 2$  mm diameter, 0.5 mm thickness) samples were placed into the Transwell inserts for the treatment groups. Untreated cells were used as a mock control. 24 h following treatment, cells were harvested in TRIzol for RNA extraction and subjected to qPCR to measure the cytokine/chemokine transcript levels.

#### GelMA-TA-PLGA Nanocomposites for Cur Delivery

Synthesis and Characterization of PLGA NPs and Cur-PLGA NPs: PLGA NPs were synthesized based on a previously published protocol with a slight modification.<sup>[94]</sup> Briefly, acid-terminated PLGA (200 mg; 50:50 lactic acid-to-glycolic acid ratio) was dissolved and stirred in 4 mL DCM. For Cur-loaded NPs, 20 mg Cur was added to the 4 mL PLGA-DCM mixture. A 25-fold volume of 1% PVA was added immediately before sonication at 50% power for 2 min with a 2 s on/ 2 s off cycle. The sonicated solution was stirred overnight in the open air to evaporate the organic solvent. Low-speed centrifugation (1000 rpm, 5 min) was performed to remove unencapsulated drug pellets, followed by washing the NPs with MilliQ water using a 100K MWCO protein concentrator. NPs were diluted 100X with MilliQ water for DLS characterization to measure their size, PDI, and zeta potential as described previously. PLGA NPs were then concentrated 10X and stored at 4 °C. Unencapsulated Cur pellets were redissolved in ethanol, and a Thermo Scientific NanoDrop One/OneC Microvolume UVvis spectrophotometer was used to measure absorbance at 425 nm. A standard calibration curve of Cur in ethanol was prepared in parallel to quantify the amount of free drug. The drug loading efficiency was calculated using the previously described equation in the earlier section.

Synthesis of GelMA-TA Hydrogel: A 10% (w/v) GelMA prepolymer solution was prepared following the previously described protocol in the earlier section. After GelMA hydrogel formation, it was treated with 100% (w/v) TA for 24 h at room temperature, based on a previously published method.<sup>[39a]</sup> After crosslinking, the hydrogel was rinsed with MilliQ water and stored at 4 °C.

Synthesis and Characterization of GelMA-TA-PLGA Nanocomposite Hydrogel: To crosslink PLGA or Cur-PLGA NPs within the GelMA-TA hydrogel, the hydrogel was fully immersed in concentrated PLGA or Cur-PLGA NP suspensions for 5 h at room temperature. After incubation, the hydrogel was thoroughly washed with MilliQ water to remove uncrosslinked NPs. The absorbance of the Cur-PLGA NP solution was measured before and after hydrogel incubation at 425 nm using a Thermo Scientific NanoDrop One/OneC Microvolume UV-vis spectrophotometer. Unloaded PLGA NPs were used as a blank to account for the background signal. Cur concentrations were determined using a standard calibration curve prepared in ethanol. The amount of Cur retained within the hydrogel was calculated based on the reduction in Cur concentration in the surrounding solution relative to its initial concentration.

XPS (AXIS Ultra DLD instrument) was employed to analyze the chemical composition of the PLGA NPs, GelMA-TA hydrogel, and GelMA-TA-PLGA nanocomposite hydrogel. A monochromatic Al K $\alpha$  X-ray at 15 kV and 10 mA served as the excitation source, and the neutral C 1s peak (C—C (H) set at 284.6 eV) was used as a reference for charge correction. Confocal microscopy (Leica TCS-SP8 Confocal Microscope with Digital Light Sheet) was used to visualize Cur-PLGA NP distribution within GelMA-TA hydrogels after crosslinking. For cross-sectional morphological analysis, GelMA

1616280.8, D. Dowbloaded from https://advaeced.onlinelibray.wiley.com/doi/10.1.002/adfm.202361881 by University Of California, Los Angeles, Wiley Commons and Conditions (https://onlinelibrary.wiley.com/terms-and-conditions) on Wiley Online Library for rules of use; OA articles are governed by the applicable Centwive Commons and Conditions (https://onlinelibrary.wiley.com/terms-and-conditions) on Wiley Online Library for rules of use; OA articles are governed by the applicable Centwive Commons and Conditions (https://onlinelibrary.wiley.com/terms-and-conditions) on Wiley Online Library for rules of use; OA articles are governed by the applicable Centwive Commons and Conditions (https://onlinelibrary.wiley.com/terms-and-conditions) on Wiley Online Library for rules of use; OA articles are governed by the applicable Centwive Commons and Conditions (https://onlinelibrary.wiley.com/terms-and-conditions) on Wiley Online Library for rules of use; OA articles are governed by the applicable Centwide Commons and Conditions (https://onlinelibrary.wiley.com/terms-and-conditions) on Wiley Online Library for rules of use; OA articles are governed by the applicable Centwide Commons and Conditions (https://onlinelibrary.wiley.com/terms-and-conditions) on Wiley Online Library for rules of use; OA articles are governed by the applicable Centwide Commons and Conditions (https://onlinelibrary.wiley.com/terms-and-conditions) on the applicable Centwide Commons and Conditions (https://onlinelibrary.wiley.com/terms-and-conditions) of the applicable Centwide Commons and Conditions (https://onlinelibrary.wiley.com/terms-and-conditions) on the applicable Centwide Commons and Conditions (https://onlinelibrary.wiley.com/terms-and-

www.afm-journal.de

and GelMA-TA hydrogels were immersed in concentrated PLGA NP solutions, and SEM analysis was performed on their cross-sectional areas. Samples were incubated in DPBS overnight, lyophilized for one day, and then fractured to expose the internal structure. The fractured surfaces were sputter-coated with gold for 60 s using a Pelco SC-7 sputter coater. SEM images were acquired using a FEI Teneo SEM at an accelerating voltage of 10 kV and a current of 0.2 nA.

Drug Release Study of Cur-PLGA Crosslinked GelMA-TA Nanocomposite Hydrogel: To evaluate drug release behavior, Cur-PLGA crosslinked GelMA-TA hydrogels were incubated in 50 mL of 1.5% (w/v)  $\beta$ -CD in DPBS at 37 °C under gentle shaking.  $\beta$ -CD was used to enhance the solubility of Cur and maintain sink conditions by forming inclusion complexes that prevent Cur precipitation and ensure sustained diffusion.<sup>[95]</sup> At predetermined time points, 1 mL of the release medium was collected and replaced with an equal volume of fresh  $\beta$ -CD-DPBS solution to maintain sink conditions. The amount of Cur released was quantified using HPLC equipped with a Shimadzu Nexcol C18 column (1.8 µm,  $50 \times 2.1$  mm) operating at a flow rate of 0.5 mL min<sup>-1</sup>, following the method described in the earlier section. This approach was necessary as the drug concentration was too low for accurate detection by UV-vis spectrophotometry. Cur concentrations were determined using a standard calibration curve prepared in ACN. The cumulative drug release was expressed as a percentage of the total Cur content initially loaded into the hydrogel.

Animals and Ethics Statement: New Zealand white rabbits (4 to 5 pounds) were purchased from Charles River Laboratory Inc. (Wilmington, MA). C57BL/6 wild-type (WT) mice (6-10 weeks age) were purchased from Jackson Laboratory (Bar Harbor, ME). The rabbits were maintained at the Harry S. Truman Memorial Veterans' Hospital animal facility, and the mice were kept at the University of Missouri (MU) School of Medicine Office of Animal Resources (OAR) facility. All animals were housed in a controlled-access. The Association for Assessment and Accreditation of Laboratory Animal Care (AAALAC) approved OAR facility, maintained in a 12:12 h light/ dark cycle, and had ad libitum access to food and water. Animals were treated in compliance with the Association for Research in Vision and Ophthalmology (ARVO) Statement for the Use of Animals in Ophthalmic and Vision Research. The Animal protocols were approved by the MU's Institutional Animal Care and Use Committees and the Harry S. Truman Memorial Veterans' Hospital. The in vivo subcutaneous studies were approved by the IACUC (ARC-2021-113) at UCLA. Male Wistar rats (250-300 g) were obtained from Charles River Laboratories (Boston, MA) and anesthetized with ~2% isoflurane.

In Vivo Biocompatibility Characterizations of OcuTAPE: After anesthesia, eight 1 cm incisions were made on the dorsal skin of each rat, and small subcutaneous pockets were created using blunt scissors. Lyophilized OcuTAPE samples, synthesized as per the previously described protocol, were implanted into these pockets, and the incisions were closed with 4–0 polypropylene sutures (n = 4). On days 7 and 14 postoperation, the rats were euthanized, and the implanted hydrogels, along with surrounding tissues, were collected for histological analysis to assess inflammatory responses. The hydrogels were fixed in 4% paraformaldehyde for 4 h, then incubated at 4 °C in 15% and 30% (w/v) sucrose solutions. The samples were embedded in Optimal Cutting Temperature (OCT) compound, frozen in liquid nitrogen, and sectioned using a Leica CM1950 cryostat. Sections (20-40 μm) were mounted on positively charged slides and processed for H&E and MT staining according to the manufacturer's instructions. IF staining was performed on rat subcutaneous tissue using rabbit anti-CD68 (ab125212, Abcam) and rabbit anti-CD3 (17617-1-AP, Proteintech) as primary antibodies. Goat anti-rabbit IgG (H+L) secondary antibodies conjugated to Alexa Fluor 594 and Alexa Fluor 488 (Invitrogen) were used to detect CD68 and CD3, respectively. DAPI was used for staining, and fluorescent images were captured using a ZEISS Axio Observer Z7 inverted microscope.

In Vivo Immediate Adhesion to Pig Conjunctiva: Under anesthesia, a Yucatan pig was used to assess the immediate adhesion of OcuTAPE (ARC-2016-085). OcuTAPE was placed on the conjunctiva of the pig, followed by 1 min pressing, then the adhesive patch was removed immediately using a tweezer to assess the adhesion.

In Vivo Adhesion to Rabbit Eyes: Rabbits were anesthetized by intramuscular injection of a cocktail of ketamine hydrochloride (50 mg kg<sup>-1</sup>) and xylazine hydrochloride (10 mg kg<sup>-1</sup>) and two drops of topical anesthetic, proparacaine hydrochloride (0.5%) onto the eye before OcuTAPE application or pathological evaluation to minimize pain and discomfort to animals. The OcuTAPE was placed on the corneoscleral junction and gently pressed against the eyelids. Only one eye (either left or right) of each animal was used for the OcuTAPE application, and contralateral eyes served as controls. Rabbit's eyes were imaged using a stereomicroscope (MZ16F; Leica Microsystems, Wetzlar, Germany) equipped with a digital camera (SpotCam RT KE, Diagnostic Instruments Inc., Sterling Heights, MI) and high-resolution confocal imaging systems SPECTRALIS (Heidelberg Engineering, Dossenheim, Germany). Rabbits were thermally supported throughout the procedure and during the anesthetic recovery period.

Induction of Intraocular Inflammation: C57BL/6 WT mice were anesthetized using ketamine (70 mg kg<sup>-1</sup>) and xylazine (10 mg kg<sup>-1</sup>) and intravitreally injected with LPS (100 ng per eye) using a 34-G needle under a dissecting ophthalmoscope. Contralateral eyes were injected with sterile DPBS and used as controls. The animals were randomly divided into five groups: i) LPS injection only, ii) LPS injection with blank OcuTAPE treatment, iii) LPS injection with Dex-loaded OcuTAPE treatment, iv) LPS injection with Dex eye drops (free drug, 0.1% ophthalmic, twice a day) treatment, and v) LPS injection with Histoacryl treatment. After 24 h of treatment, the retinal tissue was harvested and subjected to qPCR to measure the mRNA expression of proinflammatory cytokines, chemokines, and genes modulating oxidative stress. From another set of experiments, eyes cryosections were used for SOD2 and 8-OHdG immunofluorescence staining.

RNA Extraction and qPCR Analysis: Total RNA was extracted from retinal tissue using TRIzol reagent per manufacturer's instructions (Thermo Scientific, Rockford, IL). cDNA was synthesized using 1  $\mu g$  of total RNA with a Maxima first-strand cDNA synthesis kit, per the manufacturer's instructions (Thermo Scientific, Rockford, IL). The cDNA was amplified using gene-specific PCR primers using the QuantStudio 3 Real-Time PCR system (ThermoFisher Scientific, Rockford, IL). The relative expression of genes was normalized in proportion to the constitutive gene 18s RNA as an internal control and quantitatively analyzed using the  $\Delta\Delta_{CT}$  method and represented as fold change expression.

Immunofluorescence Staining: For immunostaining, 10 µm-thick retinal sections were fixed with 4% paraformaldehyde in DPBS for 15 min at room temperature. After three DPBS washes, the sections were blocked and permeabilized using 10% (v/v) goat serum containing 0.4% Triton X-100 diluted in DPBS for 2 h at room temperature. The retinal sections were then incubated with primary (anti-SOD2/8-OHdG) mouse/rabbit monoclonal antibodies (1:100 dilution) overnight at 4 °C. Following incubation, the sections were washed extensively with DPBS and incubated with anti-mouse/rabbit Alexa Fluor 488/594-conjugated secondary antibody (1:200 dilutions) for 1 h at room temperature. Tissue sections were extensively washed with DPBS and mounted with Vectashield anti-fade mounting medium containing DAPI (Vector Laboratories, Burlingame, CA). The slides were imaged using a Keyence microscope (Keyence, Itasca, IL).

Statistical Analysis: The statistical differences between experimental groups were analyzed using GraphPad Prism 10.1.2 (GraphPad Software, La Jolla, CA). The t-test (two groups), one-way analysis of variance (ANOVA) (three or more independent groups), and two-way ANOVA were used to compare the significance level between experimental groups, as indicated in the figure legends. A value of p < 0.05 was considered statistically significant. All data are expressed as mean  $\pm$  standard deviation (SD) as indicated in respective figure legends from biological replicates ( $n \ge 3$ ) unless indicated otherwise.

#### Supporting Information

Supporting Information is available from the Wiley Online Library or from the author.

## ADVANCED FUNCTIONAL MATERIALS

16163028, 0, Downloaded from https://advanced.onlinelibrary.wiley.com/doi/10.1002/adfm.202516281 by University Of California, Los Angeles, Wiley Online Library on [22:08:2025]. See the Terms and Conditions (https://onlinelibrary.wiley.com/terms-

and-conditions) on Wiley Online Library for rules of use; OA articles are governed by the applicable Creative Commons

#### Acknowledgements

The authors acknowledge Cristopher Navarro, Vy Tran, and Marian Olewine for the illustrations of this work. The authors thank Dr. Jeffrey Ardell, Amiksha S. Gandhi, and Ronald Challita for their invaluable assistance with harvesting fresh pig eyeballs and conducting the in vivo pig experiments to assess patch adhesion. The authors acknowledge Dr. Yavuz Oz for assistance with TEM imaging of the MCs. The authors acknowledge Jason Ma for his assistance with PLGA NP synthesis and data organization. The authors thank Dr. Haley Marks for help with confocal imaging and Dr. Tess De Maeseneer for assistance with SEM imaging. The authors also thank Randy Chen for supporting XPS data collection and Jim Liu for his help in validating the drug diffusion models. This work was supported by the National Institutes of Health (NIH) under grant numbers R01EB023052 (to N.A.) and R01EY032495 (to P.K.S.), and by the Department of Defense (DOD), Vision Research Program (VRP), Investigator-Initiated Research Award W81XWH-21-1-0869 (to N.A.). Additional support was provided by research start-up funds from the University of Missouri School of Medicine to P.K.S. The funders had no role in study design, data collection and analysis, decision to publish, or preparation of the manuscript.

#### **Conflict of Interest**

Prof. Annabi holds equity in GelMEDIX Inc.

#### **Data Availability Statement**

All data are available in the main text or the supplementary materials. The data that support the findings of this study are available from the corresponding author upon reasonable request.

#### **Keywords**

anti-inflammatory therapy, bioadhesive hydrogel, ocular patch, sustained drug release, tannic acid-bridged nanocomposite

Received: June 26, 2025 Revised: July 21, 2025 Published online:

- [1] a) Y. Chabria, G. P. Duffy, A. J. Lowery, R. M. Dwyer, *Biomedicines* 2021, 9, 1694;
- [2] C. Dannert, B. T. Stokke, R. S. Dias, *Polymers (Basel)* **2019**, *11*, 275.
- [3] M. A. Campea, M. J. Majcher, A. Lofts, T. Hoare, Adv. Funct. Mater. 2021, 31, 2102355.
- [4] a) G. Trujillo-de Santiago, R. Sharifi, K. Yue, E. S. Sani, S. S. Kashaf, M. M. Alvarez, J. Leijten, A. Khademhosseini, R. Dana, N. Annabi, Biomaterials 2019, 197, 345; b) M. W. Grinstaff, Biomaterials 2007, 28, 5205.
- [5] C. Jumelle, A. Yung, E. S. Sani, Y. Taketani, F. Gantin, L. Bourel, S. Wang, E. Yuksel, S. Seneca, N. Annabi, R. Dana, *Acta Biomater.* 2022, 137. 53.
- [6] a) N. Bayat, Y. Zhang, P. Falabella, R. Menefee, J. J. Whalen, M. S. Humayun, M. E. Thompson, Sci. Transl. Med. 2017, 9, aan3879; b) G. Yazdanpanah, R. Shah, R. S. S. Raghurama, K. N. Anwar, X. Shen, S. An, M. Omidi, M. I. Rosenblatt, T. Shokuhfar, A. R. Djalilian, Ocul. Surf. 2021, 21, 27; c) B. Li, J. J. Whalen, M. S. Humayun, M. E. Thompson, Adv. Funct. Mater. 2019, 30, 1907478; d) A. Fabiano, R. Bizzarri, Y. Zambito, Int. J. Nanomed. 2017, 12, 633; e) Y. Han, L.

- Jiang, H. Shi, C. Xu, M. Liu, Q. Li, L. Zheng, H. Chi, M. Wang, Z. Liu, M. You, X. J. Loh, Y. L. Wu, Z. Li, C. Li, *Bioact. Mater.* **2022**, *9*, 77; f) L. Ou, Z. Wu, X. Hu, J. Huang, Z. Yi, Z. Gong, H. Li, K. Peng, C. Shu, L. H. Koole, *Acta Biomater.* **2024**, *175*, 353; g) L. J. Luo, D. D. Nguyen, J. Y. Lai, *Mater. Sci. Eng. C Mater. Biol. Appl.* **2020**, *115*, 111095; h) A. Fernandez-Colino, D. A. Quinteros, D. A. Allemandi, A. Girotti, S. D. Palma, F. J. Arias, *Mol. Pharm.* **2017**, *14*, 4498.
- [7] a) S. Sharifi, M. M. Islam, H. Sharifi, R. Islam, D. Koza, F. Reyes-Ortega, D. Alba-Molina, P. H. Nilsson, C. H. Dohlman, T. E. Mollnes, J. Chodosh, M. Gonzalez-Andrades, Bioact. Mater. 2021, 6, 3947; b) M. Li, R. Wei, C. Liu, H. Fang, W. Yang, Y. Wang, Y. Xian, K. Zhang, Y. He, X. Zhou, Bioact. Mater. 2023, 25, 333; c) Y. A. Qian, K. J. Xu, L. L. Shen, M. L. Dai, Z. L. Zhao, Y. J. Zheng, H. O. Wang, H. L. Xie, X. Wu, D. C. Xiao, Q. X. Zheng, J. Y. Zhang, Y. Song, J. L. Shen, W. Chen, Adv. Funct. Mater. 2023, 33, 2300707; d) X. Zhao, S. Li, X. Du, W. Li, Q. Wang, D. He, J. Yuan, Bioact. Mater. 2022, 8, 196; e) F. Wang, W. Zhang, Y. Qiao, D. Shi, L. Hu, J. Cheng, J. Wu, L. Zhao, D. Li, W. Shi, L. Xie, Q. Zhou, Adv. Healthcare Mater. 2023, 12, 2300192; f) J. Liu, Y. Huang, W. Yang, X. Sun, Y. Xu, Y. Peng, W. Song, J. Yuan, L. Ren, Acta Biomater. 2022, 153, 273; g) Q. Wang, X. Zhao, F. Yu, P. H. Fang, L. Liu, X. Du, W. Li, D. He, Y. Bai, S. Li, J. Yuan, Small Methods 2024, 8, 2300996; h) H. Kabir, S. S. Mahdavi, M. J. Abdekhodaie, A. B. Rafii, M. Merati, Int. J. Biol. Macromol. 2024, 278, 134761; i) H. Lee, A. Chandrasekharan, K. Y. Seong, Y. J. Jo, S. Park, S. An, S. Lee, H. Kim, H. Ahn, S. Seo, J. S. Lee, S. Y. Yang, Bioeng. Transl. Med. 2022, 7, 10323; j) S. W. Maeng, T. Y. Park, J. S. Min, L. Jin, K. I. Joo, W. C. Park, H. J. Cha, Adv. Healthcare Mater. 2021, 10, 2100100; k) E. S. Sani, A. Kheirkhah, D. Rana, Z. M. Sun, W. Foulsham, A. Sheikhi, A. Khademhosseini, R. Dana, N. Annabi, Sci. Adv. 2019, 5, 1281.
- [8] a) S. H. Zhang, H. Zhou, C. Huang, J. G. Sun, X. Qu, Y. Lu, Chinese Chem. Lett. 2022, 33, 4321; b) J. Rosenquist, M. Folkesson, L. Hoglund, J. Pupkaite, J. Hilborn, A. Samanta, ACS Appl. Mater. Interfaces 2023, 15, 34407. c) C. Wei, J. Song, H. Tan, Biomater. Sci. 2021, 9, 7522
- [9] O. J. Uwaezuoke, P. Kumar, L. C. du Toit, N. Ally, Y. E. Choonara, ACS Omega 2024, 9, 31410.
- [10] E. Sanchez Armengol, B. Grassiri, A. M. Piras, Y. Zambito, A. Fabiano, F. Laffleur, *Int. J. Biol. Macromol.* 2024, 254, 127939.
- [11] J. Y. Lai, L. J. Luo, D. D. Nguyen, Chem. Eng. J. 2020, 402, 126190.
- [12] a) L. Zhao, Z. Shi, X. Sun, Y. Yu, X. Wang, H. Wang, T. Li, H. Zhang, X. Zhang, F. Wang, X. Qi, R. Cao, L. Xie, Q. Zhou, W. Shi, Adv. Health-care Mater. 2022, 11, 2201576; b) V. Diaz-Tome, X. Garcia-Otero, R. Varela-Fernandez, M. Martin-Pastor, A. Conde-Penedo, P. Aguiar, M. Gonzalez-Barcia, A. Fernandez-Ferreiro, F. J. Otero-Espinar, Int. J. Pharm. 2021, 597, 120318.
- [13] J. Balasubramaniam, J. K. Pandit, Drug Deliv. 2003, 10, 185.
- [14] Z. Chen, M. Yang, Q. Wang, J. Bai, C. McAlinden, E. Skiadaresi, J. Zhang, L. Pan, C. Mei, Z. Zeng, J. Yu, Y. Feng, Z. Jiang, W. Xu, H. Xu, X. Ye, H. He, Q. Wang, J. Deng, J. Huang, Carbohydr. Polym. 2021, 253, 117216.
- [15] a) L. Koivusalo, M. Kauppila, S. Samanta, V. S. Parihar, T. Ilmarinen, S. Miettinen, O. P. Oommen, H. Skottman, Biomaterials 2019, 225, 119516; b) H. Liu, X. Bi, Y. Wu, M. Pan, X. Ma, L. Mo, J. Wang, X. Li, Acta Biomater. 2021, 131, 162; c) Y. H. Cheng, M. P. Fung, Y. Q. Chen, Y. C. Chiu, J. Drug Deliv. Sci. Tec. 2024, 93, 105450.
- [16] X. Shi, T. Zhou, S. Huang, Y. Yao, P. Xu, S. Hu, C. Tu, W. Yin, C. Gao, J. Ye, Acta Biomater. 2023, 158, 266.
- [17] S. H. Sunwoo, K. H. Ha, S. Lee, N. Lu, D. H. Kim, Annu. Rev. Chem. Biomol. Eng. 2021, 12, 359; b) A. Ullah, D. Y. Kim, S. I. Lim, H.-R. J. G. Lim, Gels 2025, 11, 232.
- [18] a) C. W. McMonnies, Cont. Lens Anterior Eye 2007, 30, 37; b) S. E. Skalicky, Ocular Visual Physiology: Clinical Application, Springer, Germany 2016; c) A. Matthews, C. Hutnik, K. Hill, T. Newson, T. Chan, G. Campbell, Eye 2014, 28, 880.

16163028, 0, Downloaded from https://advanced.onlinelibrary.wiley.com/doi/10.1002/adfm.202516281 by University Of California, Los Angeles, Wiley Online Library on [22/08/2025]. See the Terms and Conditions (https://onlinelibrary.wiley.com/erms

and-conditions) on Wiley Online Library for rules of use; OA articles are governed by the applicable Creative Commons

- [19] M. Navascues-Cornago, T. Sun, M. L. Read, P. B. Morgan, Cont. Lens Anterior Eye 2022, 45, 101596.
- [20] M. Lamas, Exp. Eye Res. 2023, 236, 109673.
- [21] L. J. Luo, D. D. Nguyen, C. C. Huang, J. Y. Lai, Chem. Eng. J. 2022, 429, 132409.
- [22] D. D. Nguyen, L. J. Luo, C. J. Yang, J. Y. Lai, ACS Nano 2023, 17, 168.
- [23] Y. Zheng, K. Shariati, M. Ghovvati, S. Vo, N. Origer, T. Imahori, N. Kaneko, N. Annabi, *Biomaterials* 2023, 301, 122240.
- [24] S. Y. Z. Moghaddam, E. Biazar, J. Esmaeili, B. Kheilnezhad, F. Goleij, S. Heidari, Mini-Rev. Med. Chem. 2023, 23, 1320.
- [25] X. Chen, S. Gholizadeh, M. Ghovvati, Z. Wang, M. J. Jellen, A. Mostafavi, R. Dana, N. Annabi, AIChE J. 2023, 69, 18067.
- [26] K. Bourzac, Nature 2012, 491, S58.
- [27] C. J. Yang, D. D. Nguyen, J. Y. Lai, Adv. Sci. (Weinh) 2023, 10, 2302174.
- [28] C. Torres-Luna, X. Fan, R. Domszy, N. Hu, N. S. Wang, A. Yang, Eur. J. Pharm. Sci. 2020, 154, 105503.
- [29] Y. Shirasaki, J. Pharm. Sci. 2008, 97, 2462.
- [30] a) W. H. De Jong, Int. J. Nanomedicine (Lond) 2008, 3, 133; b) K. Cho, X. Wang, S. Nie, Z. G. Chen, D. M. Shin, Clin. Cancer Res. 2008, 14, 1310.
- [31] a) I. A. Khalil, B. Saleh, D. M. Ibrahim, C. Jumelle, A. Yung, R. Dana, N. Annabi, *Biomater. Sci.* 2020, 8, 5196; b) A. Yung, Y. C. Liu, S. Gholizadeh, A. Naderi, F. Kahale, N. Annabi, R. Dana, *Invest. Ophth. Vis. Sci.* 2022, 63, 4149.
- [32] F. Wahid, C. Zhong, H. S. Wang, X. H. Hu, L. Q. Chu, *Polymers (Basel)* 2017, 9, 636.
- [33] Y. Zheng, A. Baidya, N. Annabi, Bioact. Mater. 2023, 29, 214.
- [34] a) G. E. Amiel, I. Sukhotnik, B. Kawar, L. Siplovich, J. Am. Coll. Surg. 1999, 189, 21; b) U.S. Food and Drug Administration, Histoacryl and Histoacryl Blue Topical Skin Adhesive—Premarket Approval (PMA) Summary, U.S. Department of Health and Human Services, Silver Spring 2007, Available online: https://www.accessdata.fda.gov/cdrh\_docs/pdf5/P050013c.pdf.
- [35] Baxter Healthcare Corporation, Highlights of Prescribing Information, Baxter Healthcare Corporation, Deerfield, IL 2019, Available online: https://baxterpi.com/pi-pdf/Tisseel\_PI.pdf.
- [36] a) H. A. Shnawa, M. N. Khalaf, Y. Jahani, A. A. H. Taobi, J. Mater. Sci. Appl. 2015, 6, 360; b) S. Sakai, K. Kawakami, Acta Biomater. 2007, 3, 405
- [37] a) S. Q. Bian, L. Z. Hao, X. Qiu, J. Wu, H. Chang, G. M. Kuang, S. Zhang, X. H. Hu, Y. K. Dai, Z. Y. Zhou, F. L. Huang, C. Liu, X. N. Zou, W. G. Liu, W. W. Lu, H. B. Pan, X. L. Zhao, Adv. Funct. Mater. 2022, 32, 2207741; b) Y. Zhan, W. Fu, Y. Xing, X. Ma, C. Chen, Mater. Sci. Eng. C Mater. Biol. Appl. 2021, 127, 112208.
- [38] K. Chen, Q. Lin, L. Wang, Z. Zhuang, Y. Zhang, D. Huang, H. Wang, ACS Appl. Mater. Interfaces 2021, 13, 9748.
- [39] a) B. Liu, Y. Wang, Y. Miao, X. Zhang, Z. Fan, G. Singh, X. Zhang, K. Xu, B. Li, Z. Hu, M. Xing, Biomaterials 2018, 171, 83; b) M. Shin, J. H. Ryu, J. P. Park, K. Kim, J. W. Yang, H. Lee, Adv. Funct. Mater. 2015, 25, 1270; c) X. Du, L. Wu, H. Yan, L. Qu, L. Wang, X. Wang, S. Ren, D. Kong, L. Wang, ACS Biomater. Sci. Eng. 2019, 5, 2610; d) H. L. Fan, L. Wang, X. D. Feng, Y. Z. Bu, D. C. Wu, Z. X. Jin, Macromolecules 2017, 50, 666.
- [40] K. A. Vakalopoulos, Z. Wu, L. Kroese, G. J. Kleinrensink, J. Jeekel, R. Vendamme, D. Dodou, J. F. Lange, Ann. Surg. 2015, 261, 323.
- [41] C. Doria, S. Vaccino, Expert Opin. Biol. Ther. 2009, 9, 243.
- [42] a) S. Ozawa, AORN J 2013, 98, 461; b) Baxter Healthcare Corporation, COSEAL Surgical Sealant Instructions for Use, Document No. 0725395, Baxter Healthcare Corporation, Deerfield, IL 2014, Available online: https://www.advancedsurgery.baxter.com/sites/g/files/ebysai3391/files/2019-02/0725395\_10SEP2014\_Coseal\_IFU1.pdf.
- [43] K. L. Yeh, S. H. Wu, C. S. Fuh, Y. H. Huang, C. S. Chen, S. S. Wu, World J. Clin. Cases 2022, 10, 11178.
- [44] W. D. Spotnitz, S. Burks, Transfusion 2012, 52, 2243.
- [45] P. Weinrauch, S. Kermeci, J. Med. Cases 2013, 4, 608.

- [46] S. Madler, C. Bich, D. Touboul, R. Zenobi, J. Mass Spectrom. 2009, 44, 694.
- [47] W. H. Coles, P. A. Jaros, Br. J. Ophthalmol. 1984, 68, 549.
- [48] H. Yuk, C. E. Varela, C. S. Nabzdyk, X. Mao, R. F. Padera, E. T. Roche, X. Zhao, *Nature* 2019, 575, 169.
- [49] J. Li, A. D. Celiz, J. Yang, Q. Yang, I. Wamala, W. Whyte, B. R. Seo, N. V. Vasilyev, J. J. Vlassak, Z. Suo, D. J. Mooney, *Science* 2017, 357, 378.
- [50] a) N. V. Saraiya, D. A. Goldstein, Expert Opin. Pharmacother. 2011, 12, 1127; b) A. Alm, Clin. Ophthalmol. 2014, 8, 1967.
- [51] H. T. Huang, X. L. Zhang, J. H. Yu, J. P. Zeng, P. R. Chang, H. B. Xu, J. Huang, Colloid Surface B 2013, 110, 59.
- [52] D. Klose, F. Siepmann, K. Elkharraz, S. Krenzlin, J. Siepmann, Int. J. Pharm. 2006, 314, 198.
- [53] a) M. Y. Levy, S. Benita, Int. J. Pharm. 1990, 66, 29; b) P. Saarinen-Savolainen, T. Järvinen, H. Taipale, A. Urtti, Int. J. Pharm. 1997, 159, 27
- [54] a) J. R. Occhipinti, M. A. Mosier, J. LaMotte, G. T. Monji, Curr. Eye Res. 1988, 7, 995; b) W. R. Webber, D. P. Jones, Med. Biol. Eng. Comput. 1986, 24, 386.
- [55] C. J. Rijcken, T. F. Veldhuis, A. Ramzi, J. D. Meeldijk, C. F. van Nostrum, W. E. Hennink, Biomacromolecules 2005, 6, 2343.
- [56] P. J. Moncure, Z. C. Simon, J. E. Millstone, J. E. Laaser, J. Phys. Chem. B 2022, 126, 4132.
- [57] W. M. Moreira, P. V. Viotti, M. G. A. Vieira, C. M. D. G. Baptista, M. H. N. O. Scaliante, M. L. Gimenes, Sustain. Chem. Pharm. 2022, 27, 100653.
- [58] M. Kalam, M. S. Humayun, N. Parvez, S. Yadav, A. Garg, S. Amin, Y. Sultana, A. Ali, J. Cont. J. Pharm. Sci. 2007, 1, 30.
- [59] V. Papadopoulou, K. Kosmidis, M. Vlachou, P. Macheras, Int. J. Pharm. 2006, 309, 44.
- [60] Q. Sun, Z. Liu, C. Xie, L. Hu, H. Li, Y. Ge, L. Lin, B. Tang, Colloids Surf. B Biointerfaces 2023, 222, 113102.
- [61] C. Chen, H. Yang, X. Yang, Q. Ma, RSC Adv. 2022, 12, 7689.
- [62] D. Lee, H. Hwang, J. S. Kim, J. Park, D. Youn, D. Kim, J. Hahn, M. Seo, H. Lee, ACS Appl. Mater. Interfaces 2020, 12, 20933.
- [63] B. N. Narasimhan, G. S. Deijs, S. Manuguri, M. S. H. Ting, M. A. K. Williams, J. Malmström, Nanoscale Adv 2021, 3, 2934.
- [64] M. A. Hameed, F. Al-Aizari, B. Thamer, Colloids Surf. A 2024, 684, 133130.
- [65] A. K. Jaiswal, R. V. Dhumal, J. R. Bellare, G. R. Vanage, Drug Deliv. Transl. Res. 2013, 3, 504.
- [66] S. Ellis, E. J. Lin, D. Tartar, Curr. Dermatol. Rep. 2018, 7, 350.
- [67] K. Parsi, M. Kang, A. Yang, S. Kossard, Phlebology 2020, 35, 115.
- [68] a) G. J. Mattamal, Expert Rev. Med. Devices 2008, 5, 41;
- [69] a) H. Li, B. Li, Y. Zheng, Int. J. Mol. Med. 2024, 53, 45; b) S. Singh, P. K. Singh, A. Jha, P. Naik, J. Joseph, S. Giri, A. Kumar, Cell Rep. Medicine 2021, 2, 100277.
- [70] a) M. H. Mursalin, R. Astley, P. S. Coburn, F. C. Miller, M. C. Callegan, Exp. Eye Res. 2022, 224, 109213; b) D. Talreja, P. K. Singh, A. Kumar, Invest. Ophthalmol. Vis. Sci. 2015, 56, 1719.
- [71] G. Pascual, S. Sotomayor, M. Rodriguez, B. Perez-Kohler, A. Kuhnhardt, M. Fernandez-Gutierrez, J. San Roman, J. M. Bellon, *PLoS One* 2016, 11, 0157920.
- [72] J. Chang, P. McCluskey, D. Wakefield, Clinical Exp. Ophthalmol. 2012, 40, 821.
- [73] S. Raghava, M. Hammond, U. B. Kompella, Expert Opin. Drug Deliv. 2004, 1, 99.
- [74] L. Ung, U. Pattamatta, N. Carnt, J. L. Wilkinson-Berka, G. Liew, A. J. R. White, Clin. Sci. 2017, 131, 2865.
- [75] a) A. Shoham, M. Hadziahmetovic, J. L. Dunaief, M. B. Mydlarski, H. M. Schipper, Free Radic. Biol. Med. 2008, 45, 1047; b) O. A. Oduntan, K. P. Mashige, Afr. Vis. Eye Health J. 2011, 70, 191.
- [76] M. A. Babizhayev, Cell. Biochem. Funct. 2011, 29, 183.
- [77] S. Beatty, H. Koh, M. Phil, D. Henson, M. Boulton, Surv. Ophthalmol. 2000. 45, 115.





www.afm-journal.de

16163028, 0, Downloaded from https://advanced.onlinelibrary.wiley.com/doi/10.1002/adfm.202516281 by University Of California, Los Angeles, Wiley Online Library on [22/08/2025]. See the Terms

and Conditions

for rules of use; OA

articles are governed by the applicable Creative Commons

- [78] a) S. Seen, L. Tong, Acta Ophthalmol. 2018, 96, 412; b) H. L. Bui, Y. H. Su, C. J. Yang, C. J. Huang, J. Y. Lai, J. Nanobiotechnol. 2024, 22, 160; c) S. Ghosh, Y. H. Su, C. J. Yang, J. Y. Lai, J. Small. Structures. 2025, 6, 2400484.
- [79] A. Izzotti, A. Bagnis, S. C. Sacca, Mutat Res 2006, 612, 105.
- [80] S. Iwata, Y. Fukaya, K. Nakazawa, T. Okuda, J. Ocul. Pharmacol. 1987, 3, 227.
- [81] A. Aranda, L. Sequedo, L. Tolosa, G. Quintas, E. Burello, J. V. Castell, L. Gombau, Toxicol. In Vitro 2013, 27, 954.
- [82] J. Arauz, E. Ramos-Tovar, P. Muriel, Ann. Hepatol. 2016, 15, 160.
- [83] A. Dammak, C. Pastrana, A. Martin-Gil, C. Carpena-Torres, A. Peral Cerda, M. Simovart, P. Alarma, F. Huete-Toral, G. Carracedo, *Biomedicines* 2023, 11, 292.
- [84] B. Zheng, D. J. McClements, Molecules 2020, 25, 2791.
- [85] J. Shi, R. Zhang, J. Zhou, W. Yim, J. V. Jokerst, Y. Zhang, B. W. Mansel, N. Yang, Y. Zhang, J. Ma, ACS Appl. Bio Mater. 2022, 5, 1319.
- [86] a) H. Y. Chung, R. H. Grubbs, Macromolecules 2012, 45, 9666; b) B. Kong, R. Liu, Y. Cheng, Y. Shang, D. Zhang, H. Gu, Y. Zhao, W. Xu, Adv. Sci. (Weinh) 2022, 9, 2203096.
- [87] P. Thoniyot, M. J. Tan, A. A. Karim, D. J. Young, X. J. Loh, Adv. Sci. (Weinh) 2015, 2, 1400010.

- [88] M. Ghovvati, S. Baghdasarian, A. Baidya, J. Dhal, N. Annabi, J. Biomed. Mater. Res. B Appl. Biomater. 2022, 110, 1511.
- [89] S. B. Kedare, R. P. Singh, J. Food Sci. Technol. 2011, 48, 412.
- [90] M. Bagheri, J. Bresseleers, A. Varela-Moreira, O. Sandre, S. A. Meeuwissen, R. M. Schiffelers, J. M. Metselaar, C. F. van Nostrum, J. C. M. van Hest, W. E. Hennink, *Langmuir* 2018, 34, 15495.
- [91] R. Ferrari, M. Callari, D. Moscatelli, RSC Adv. 2015, 5, 67475.
- [92] a) O. Soga, C. F. van Nostrum, M. Fens, C. J. Rijcken, R. M. Schiffelers, G. Storm, W. E. Hennink, J Control Release 2005, 103, 341; b) M. Talelli, M. Iman, A. K. Varkouhi, C. J. F. Rijcken, R. M. Schiffelers, T. Etrych, K. Ulbrich, C. F. van Nostrum, T. Lammers, G. Storm, J. Biomaterials 2010, 31, 7797.
- [93] B. Srividya, R. M. Cardoza, P. D. Amin, J. Control Release 2001, 73, 205.
- [94] X. Zhang, M. M. Hasani-Sadrabadi, J. Zarubova, E. Dashtimighadam, R. Haghniaz, A. Khademhosseini, M. J. Butte, A. Moshaverinia, T. Aghaloo, S. Li, *Matter* 2022, 5, 666.
- [95] S. Kolay, N. K. Apohan, E. Babuc, G. Gun, AAPS PharmSciTech. 2025, 26, 99